European Journal of Medicinal Chemistry 268 (2024) 116202

Contents lists available at ScienceDirect

European Journal of Medicinal Chemistry

journal homepage: www.elsevier.com/locate/ejmech

Research paper

Design, synthesis, and biological evaluation of first-in-class indomethacin-based PROTACs degrading SARS-CoV-2 main protease and with broad-spectrum antiviral activity

Jenny Desantis [a,1], Alessandro Bazzacco [b,1], Michela Eleuteri [a], Sara Tuci [b], Elisa Bianconi [c], Antonio Macchiarulo [c], Beatrice Mercorelli [b,***], Arianna Loregian [b,**,2], Laura Goracci [a,*,2]

[a] Department of Chemistry, Biology, and Biotechnology, University of Perugia, Italy
[b] Department of Molecular Medicine, University of Padua, Padua, Italy
[c] Department of Pharmaceutical Science, University of Perugia, Italy

ARTICLE INFO

Handling Editor: Dr. Z Liu

Keywords:
PROTAC
SARS-CoV-2
Main protease (M^{pro})
Antiviral
Targeted protein degradation

ABSTRACT

To date, Proteolysis Targeting Chimera (PROTAC) technology has been successfully applied to mediate proteasomal-induced degradation of several pharmaceutical targets mainly related to oncology, immune disorders, and neurodegenerative diseases. On the other hand, its exploitation in the field of antiviral drug discovery is still in its infancy. Recently, we described two indomethacin (INM)-based PROTACs displaying broad-spectrum antiviral activity against coronaviruses. Here, we report the design, synthesis, and characterization of a novel series of INM-based PROTACs that recruit either Von-Hippel Lindau (VHL) or cereblon (CRBN) E3 ligases. The panel of INM-based PROTACs was also enlarged by varying the linker moiety. The antiviral activity resulted very susceptible to this modification, particularly for PROTACs hijacking VHL as E3 ligase, with one piperazine-based compound (PROTAC **6**) showing potent anti-SARS-CoV-2 activity in infected human lung cells. Interestingly, degradation assays in both uninfected and virus-infected cells with the most promising PROTACs emerged so far (PROTACs **5** and **6**) demonstrated that INM-PROTACs do not degrade human PGES-2 protein, as initially hypothesized, but induce the concentration-dependent degradation of SARS-CoV-2 main protease (M^{pro}) both in M^{pro}-transfected and in SARS-CoV-2-infected cells. Importantly, thanks to the target degradation, INM-PROTACs exhibited a considerable enhancement in antiviral activity with respect to indomethacin, with EC_{50} values in the low-micromolar/nanomolar range. Finally, kinetic solubility as well as metabolic and chemical stability were measured for PROTACs **5** and **6**. Altogether, the identification of INM-based PROTACs as the first class of SARS-CoV-2 M^{pro} degraders demonstrating activity also in SARS-CoV-2-infected cells represents a significant advance in the development of effective, broad-spectrum anti-coronavirus strategies.

1. Introduction

Targeted protein degradation (TPD), exemplified through proteolysis targeting chimeras (PROTACs), is receiving a great deal of attention from both industry and academia as a new generation of therapeutics based on the removal of disease-related target proteins [1–5]. Structurally, a PROTAC is a hetero-bifunctional molecule composed of two ligands, one binding to a protein of interest (POI) and the other one recruiting an E3 ubiquitin ligase, connected through a linker. Thus, the chemically induced proximity between POI and E3 ligase leads to the formation of a ternary complex (POI-PROTAC-E3 ligase) that can trigger the ubiquitination of the POI and its subsequent degradation via the ubiquitin proteasomal system [6,7]. Since its first conceptualization in 2001 by Crews and coworkers [8], thousands of PROTACs have been reported becoming a new paradigm in drug discovery. Among them, PROTACs **ARV-110** and **ARV-471** were the first oral PROTACs to be

* Corresponding author.
** Corresponding author.
*** Corresponding author.
E-mail addresses: beatrice.mercorelli@unipd.it (B. Mercorelli), arianna.loregian@unipd.it (A. Loregian), laura.goracci@unipg.it (L. Goracci).
[1] These authors contributed equally.
[2] These authors contributed equally.

https://doi.org/10.1016/j.ejmech.2024.116202
Received 15 November 2023; Received in revised form 29 January 2024; Accepted 31 January 2024
Available online 6 February 2024

advanced to clinical investigation for the treatment of prostate and breast cancer, respectively, but several further PROTACs candidates then followed the same fate, thus demonstrating how this technology is quickly going to approach to the clinics [9–13].

Differently from classical protein inhibitors, PROTACs work with a catalytic and event-driven mechanism of action that awards them of relevant advantages, such as abolishing all the POI functions at once, achieving a more prolonged biologic effect, and reducing the dose and thus off-target side effects and toxicity [14]. To date, PROTAC technology has been widely and successfully applied against oncology-related target proteins as well as in the case of immune disorders, neurodegenerative, and cardiovascular diseases [10,15,16]. On the other hand, its exploitation in the antiviral field is still marginal [17–21]. Only recently, TPD technology has started to be considered as a potential and emerging weapon against pathogenic viruses by promoting the degradation of either viral or host-related protein targets [22–30]. Besides the common advantages that TPD may provide over the traditional small-molecule inhibitors, antiviral PROTACs can benefit of high selectivity toward pathogen-specific isoforms, but above all could be less prone to the induction of drug resistance, since either mutations or changes in abundance of POI might occur less frequently [20]. One challenge of applying TPD to antiviral targets is represented by the ligand selection. Indeed, for most of the antiviral PROTACs developed so far, the ligand was an enzymatic inhibitor of the POI [23,30]. However, it might be difficult to discriminate between the antiviral activity due to the inhibition of the POI in the context of infection and the antiviral activity exclusively linked to the degradation of the POI, since when inhibited by the ligand, a reduction in its levels occurs in the context of infection. This can be overcome by using a ligand not acting as an enzymatic inhibitor as a warhead, not inducing by itself a reduction of the POI in the context of infection.

Given the severity of the SARS-CoV-2 outbreak and considering the pressing need to counteract new potentially emerging pathogenic variants [31], we previously decided to exploit PROTAC technology in the search for anti-coronavirus PROTACs endowed with an innovative mechanism of action [27]. Indeed, as mentioned before, PROTACs may achieve antiviral activity through the degradation of targets involved in virus replication differently from the target inhibition exploited by the anti-SARS-CoV-2 drugs licensed so far (molnupiravir, paxlovid) [32,33] or by the multitude of antivirals identified in record-breaking times by the research community [34–37]. In this context, small-molecule main protease (M^{pro}) inhibitors [38–45], papain-like protease inhibitors [46–48], RNA-dependent RNA polymerase inhibitors [49,50], entry targeting inhibitors [51], and non-structural proteins inhibitors [52] emerged as the most promising anti-SARS-CoV-2 strategies.

We recently proposed the first PROTAC application of indomethacin (INM)-based degraders endowed with SARS-CoV-2 inhibitory activity [27]. In particular, the design of the reported PROTACs was based on the weak anti-SARS-CoV-2 compound indomethacin (EC_{50} ~ 100 μM), which is a well-known, non-steroidal anti-inflammatory drug that non-selectively inhibits COX-1 and COX-2 enzymes. Although with a mechanism of action still unclear, INM has been shown to also possess broad-spectrum antiviral activity against different unrelated viruses, including SARS-CoV [53], herpesviruses [54], cytomegalovirus [55], and hepatitis B virus [56]. More recently, its activity against SARS-CoV-2 has been also investigated in *in vitro*, *in vivo,* and clinical studies [57–60]. Among the possible mechanisms that have been hypothesized, one involves the biosynthetic pathway of prostaglandin [58,59,61,62]. Indeed, INM inhibits the prostaglandin E synthase type 2 (PGES-2) [63], a host protein found as an interactor of nsp7 protein of SARS-CoV-2 in a protein-protein interaction screening [61,62]. The interaction between nsp7 and PGES-2 was also highlighted by Gordon et al. as a potential pan-CoV antiviral target, since it was found conserved across the three highly pathogenic CoVs SARS-CoV, SARS-CoV-2, and MERS-CoV [61,62]. Thus, in 2021 aiming at investigating whether PROTAC technology could represent a valid approach also in the search for anti-CoVs agents, we synthesized and tested four INM-based PROTACs for anti-SARS-CoV-2 activity [27]. Among them, PROTACs **3** [27] and **5** [27] (Fig. 1), both hijacking Von-Hippel Lindau (VHL) as E3 ligase and differing only in the linker composition, displayed an almost 5-fold improved ability compared to INM in inhibiting SARS-CoV-2 replication in infected cells (EC_{50} = 18.1 and 21.5 μM, respectively, *versus* 94.9 μM for INM), coupled with a discrete Selectivity Index (SI) (SI > 11 and > 12, respectively) [27]. Moreover, they exhibited broad-spectrum activity encompassing also endemic human coronaviruses (HCoVs), i.e., the *β*-coronavirus HCoV-OC43 and the *α*-coronavirus HCoV-229E (with EC_{50} = 4.7–2.5 μM and 36.5–3.2 μM, respectively) [27]. To note, seven types of coronaviruses infecting humans have been identified so far; among them, besides the three highly pathogenic coronaviruses SARS-CoV, MERS-CoV and SARS-CoV-2, four seasonal coronaviruses are also known, i.e. OC43, 229E, NL63, and HKU1 [64].

In the present work, the length, flexibility, and geometry of the linker connecting INM and VHL E3 ligase binding moiety were further investigated (PROTACs **6–11**) along with the exploration of cereblon (CRBN) as another E3 ligase (PROTACs **12–14**). Their design, synthesis, and biological activity are described. Moreover, an in-depth exploration on the PROTAC-mediated mechanism of action, target degradation, and physico-chemical/ADME properties are also reported.

2. Results and discussion

2.1. Design of second-generation INM-based PROTACs

Considering the pivotal role of the PROTAC linker moiety in the formation of a productive ternary complex (POI-PROTAC-E3), and thus in the POI degradation efficiency, but also in the modulation of the physico-chemical properties of the final degrader [65,66], we designed and synthesized a new array of INM-based PROTACs. In particular, we conjugated INM and VHL E3 ligase ligand through piperazine-containing linkers (as in PROTAC **5** [27]) exploiting either aliphatic or polyethylenglycol(PEG)ylated chains of different length, leading to PROTACs **6–11** (Table 1). Indeed, as different studies suggested, the insertion of piperazine rings in the linker may help in increasing the solubility as well as the metabolic stability of PROTACs [65,66].

Considering that alternative E3 ligases may offer several distinct advantages including superior activity [67], we decided to investigate also a CRBN E3 ligase ligand, i.e. thalidomide. Indeed, CRBN along with VHL represent the most popular and generally used E3 ligases to design PROTACs owing their ubiquitous expression in human body [68,69]. Thus, in a preliminary set of PROTACs INM was combined to the thalidomide moiety by using aliphatic linkers of variable length affording PROTACs **12–14** (Table 1). In particular, a similar range in atom linker length to the VHL-addressing series was investigated (6–12 *vs* 6–15, Table 1).

2.2. Chemistry

The synthesis of PROTACs **6** [66], **7** [66], **8**, and **9** [66] was performed according to Scheme 1. In particular, INM was coupled with the suitable intermediate, in which the VHL ligand was decorated with the proper linker, by amidation reaction performed in the presence of 1-[bis(dimethylamino)methylene]-1*H*-1,2,3-triazolo[4,5-*b*]pyridinium 3-oxid hexafluorophosphate (HATU) and *N,N*-diisopropylethylamine (DIPEA) at room temperature in DMF.

As reported in Scheme 2, the VHL-containing linker intermediates **20** [65] and **21** [65] used for the synthesis of target PROTACs **6** and **7**, respectively, were prepared starting from VHL ligand **17**. Indeed, **17** was first coupled with the appropriate *N*-Boc protected piperazine carboxylic acid derivatives (commercially available) through HATU-mediated amidation reaction (intermediates **18–19**) and then successively

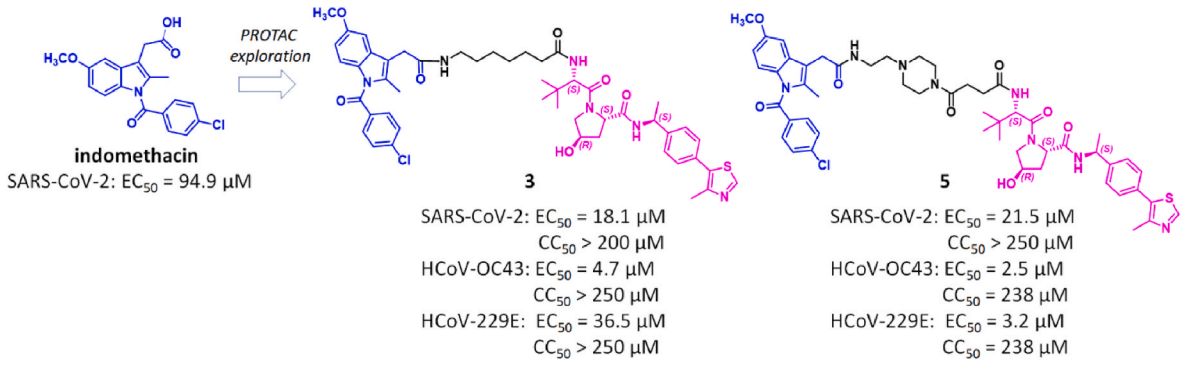

Fig. 1. Chemical structures of INM and previously reported INM-based PROTACs **3** and **5** [27]. The EC_{50} value represents the compound concentration that inhibits 50 % of viral replication. The CC_{50} value represents the compound concentration that reduces cell viability by 50 %.

Table 1
Anti-CoVs activity and cytotoxicity of INM-based PROTACs.

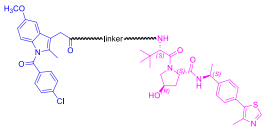

Compd	Linker	Atom linker length	CC_{50}[a] Vero E6 (μM)	EC_{50}[b] (μM) (CI)[c] SARS-CoV-2/NL/2020	CC_{50} MRC-5 (μM)	EC_{50} (μM) (CI)	
						HCoV- OC43	HCoV- 229E
3[d]	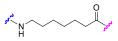	8	>200	18.1 (7.1–46.4)	>250	4.7 (1.1–18.1)	36.5 (20.1–70.3)
5[d]	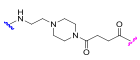	11	>250	21.5 (11.2–43.4)	238 ± 17	2.5 (0.8–7.5)	3.2 (1.4–7.1)
6		6	>125	10.8 (8.0–14.4)	>125	1.6 (0.9–2.8)	6.5 (4.2–10.0)
7		7	>125	>25	13.5 ± 0.7	ND	ND
8	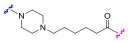	10	>125	>25	20.0 ± 7.1	ND	ND
9	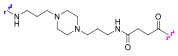	16	>125	>25	>125	16.0 (8.3–31.7)	>25
10	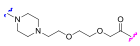	12	>125	>25	22.0 ± 5.7	ND	ND
11	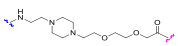	15	>125	>25	12.3 ± 0.4	ND	ND
	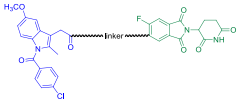						
12		6	>125	>25	ND	ND	ND
13	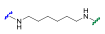	8	>125	>25	ND	ND	ND
14	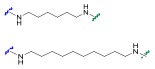	12	>125	>25	ND	ND	ND
BOC[e]	–	–	>500	22.0 ± 2.6	ND	ND	ND
INM[d]	–	–	>500	95.1 ± 9.2	ND	ND	ND

ND, Not Determined.
[a] 50 % Cytotoxic Concentration, the compound concentration that reduces cell viability by 50 %, as determined by MTT assay in Vero E6 or MRC-5 cells at 72 h.
[b] 50 % Effective Concentration, the compound concentration that inhibits 50 % of plaque formation, as determined by PRAs against SARS-CoV-2 in Vero E6 cells or different HCoV strains in MRC-5 cells. For all PROTACs, reported values represent data derived from n = 3 independent experiments in duplicate. For BOC and INM reported values represent mean ± SD of data derived from n = 2 independent experiments in duplicate.
[c] Confidence Interval, 95 % Profile likelihood, calculated with GraphPad Prism 8.0 software.
[d] Data reported in Ref. [27].
[e] Data reported in Ref. [75].

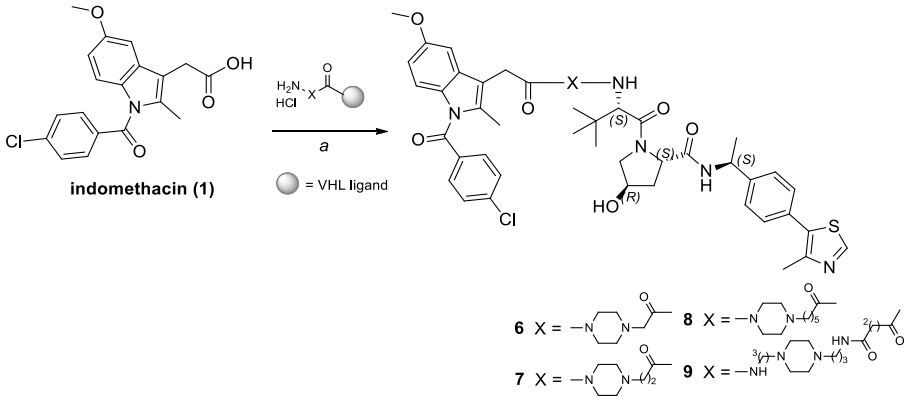

Scheme 1. Synthesis of PROTACs **6–9**. *Reagents and conditions*: (a) HATU, DIPEA, rt, dry DMF, 3–18 h. VHL: Von Hippel Lindau ligand.

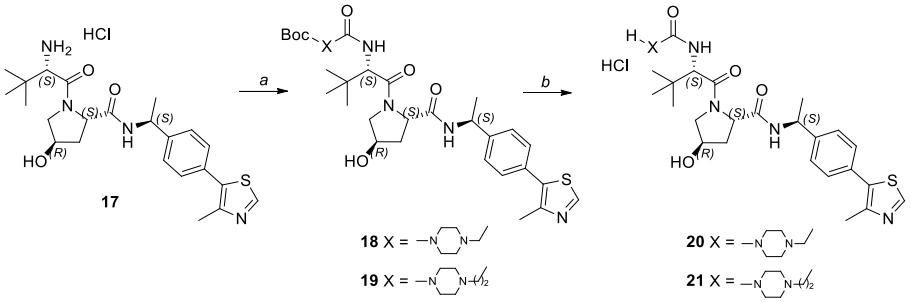

Scheme 2. Synthesis of intermediates **20–21**. *Reagents and conditions*: a) appropriate *N*-Boc piperazine carboxylic acid derivative, HATU, DIPEA, dry DMF, rt, 1 h; b) HCl 4 N in dioxane, rt, 2 h.

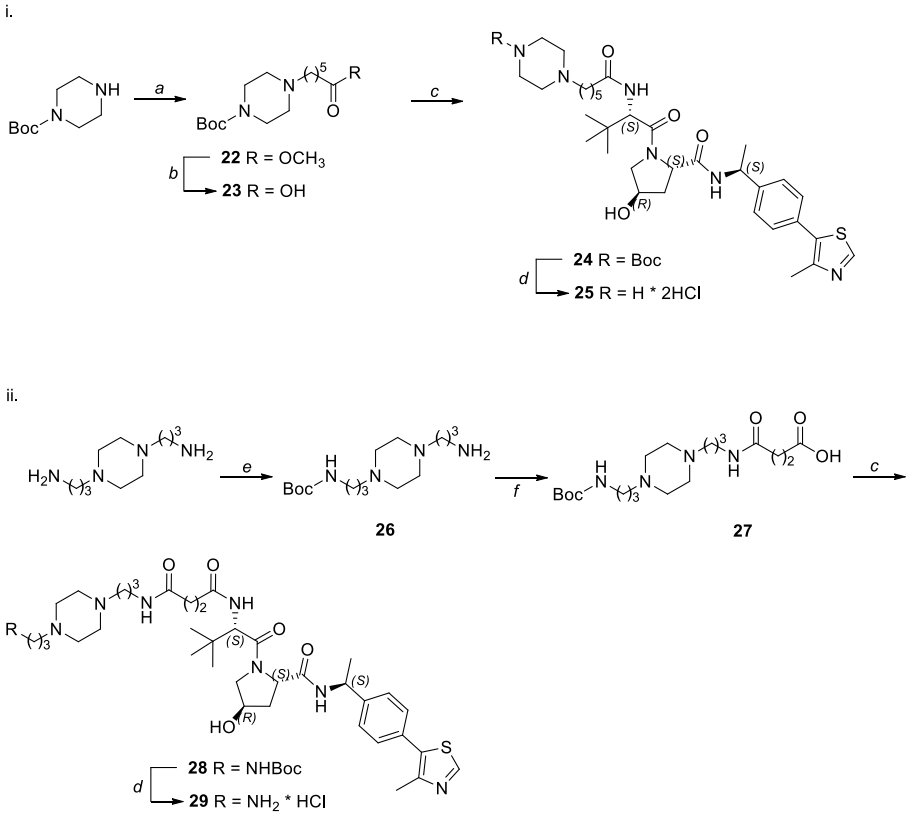

Scheme 3. Synthesis of intermediates **25** and **29**. *Reagents and conditions*: a) methyl 6-bromo esanoate, Et_3N, dry THF, rt, 18 h; b) LiOH, THF:H_2O (2:1), rt, 3 h; c) **17** (VHL ligand), HATU, DIPEA, dry DMF, rt, 3–18 h; d) HCl 4 N in dioxane, rt, 3–18 h; e) Boc_2O, dry MeOH, rt, 24 h; f) succinic anhydride, dry DCM, rt, 4 h.

deprotected to afford the suitable intermediates **21**–**21** (Scheme 2).

The VHL-containing linker intermediates **25** [66] and **29** [66] used for the synthesis of target PROTACs **8** and **9** were synthesized as previously described as reported in Scheme 3. In particular, intermediate **25** was prepared starting from *N*-Boc piperazine, which was reacted with methyl 6-bromo esanoate in the presence of Et_3N at room temperature to afford compound **22**. Then, the basic hydrolysis of methyl ester derivative **22** gave carboxylic acid derivative **23**, which after amidation reaction with VHL ligand **17** and successive *N*-Boc deprotection reaction furnished intermediate **25**. Intermediate **29** was instead prepared starting from **26** [70] firstly reacted with succinic anhydride to give compound **27**, which was then coupled by amidation reaction with VHL ligand **17** to afford compound **28**. The final *N*-Boc deprotection reaction gave intermediate **29**.

The synthesis of INM-based PROTACs **10** [66] and **11** [66] was performed as previously described according to Scheme 4. Indeed, intermediates **30** and **31** were prepared starting from **1** coupled by HATU-mediated amidation reaction using the appropriate piperazine derivative. Their successive *N*-Boc deprotection reaction led to intermediates **32** and **33**, which after substitution reaction with the VHL-linker intermediate **35** gave PROTACs **10** and **11**. The VHL ligand functionalized with an iodo-containing PEG linker (compound **35** [66]) was prepared as previously described by coupling VHL ligand **17** with 2-(2-(2-chloroethoxy)ethoxy)acetic acid by HATU-mediated amidation reaction to give chloro derivative **34** and then subjected to substitution reaction in presence of NaI to afford the corresponding iodo derivate **35**.

The CRBN-addressing PROTACs **12–14** were synthesized as depicted in Scheme 5 by HATU-mediated amidation reaction between **1** and the appropriated CRBN-linker intermediate (**40–42**). Intermediates **40–42** were in turn prepared by substitution reaction of **36**, prepared by reacting 4,5-difluorophtalic anhydride and 3-aminopiperidin-2,6-dione hydrochloride, with the suitable *N*-Boc protected di amino aliphatic chain in presence of DIPEA at 110 °C in DMSO (**37–39**), followed by Boc-deprotection reaction.

For the most promising compounds emerged from the biological characterization (PROTACs **5** and **6**), we synthesized also the corresponding inactive epimeric PROTACs (**15** and **16**) to be included as negative controls in *in vitro* assays, by replacing the *trans*-hydroxyproline (Hyp) in the VHL ligand moiety with a *cis*-Hyp, known to abrogate binding to VHL [71]. In particular, the synthesis of compound **15** (the negative controls for PROTAC **5**) was performed according to Scheme 6, in which intermediate **33** was reacted with succinic anhydride to afford **43**, which was then coupled by HATU-mediated amidation reaction with the *cis*-Hyp derivative **44** to give the target compound **15**.

The synthesis of compound **16** (the negative control for PROTAC **6**) was performed according to Scheme 7. In particular, INM was coupled with the suitable VHL-based intermediate **46** by HATU-mediated amidation reaction. The VHL-containing linker intermediate **46** used for the synthesis of target compound **16** was prepared starting from the *cis*-Hyp derivative **44**, which was first coupled with the appropriate *N*-Boc protected carboxylic acid derivative through HATU-mediated amidation reaction (intermediate **45**) and then successively deprotected to afford the intermediate **46** (Scheme 7).

Interestingly, the VHL ligand **17** [72] used for the synthesis of

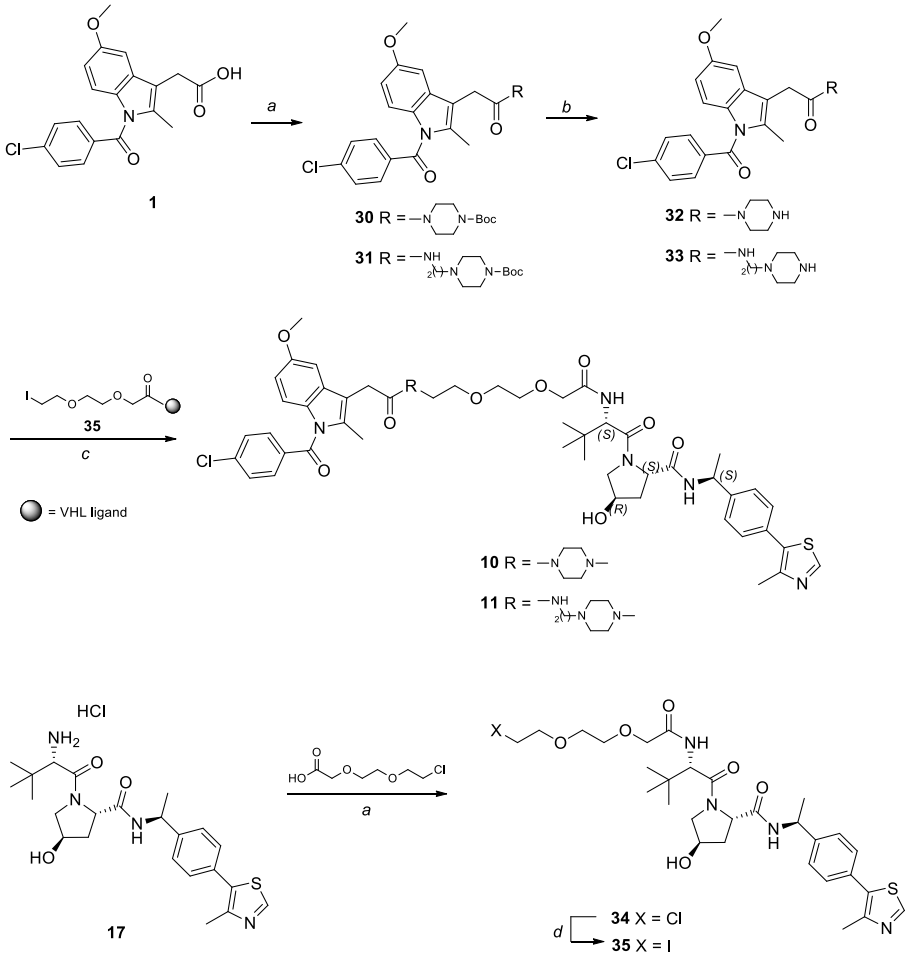

Scheme 4. Synthesis of PROTACs **10–11**. *Reagents and conditions*: (a) HATU, DIPEA, dry DMF, rt, 3 h; (b) HCl 4 N in dioxane, rt, 3–6 h; (c) DIPEA, dry DMF/dry DMSO (1:1), 80 °C, 18 h; (d) NaI, dry acetone, reflux, 48 h.

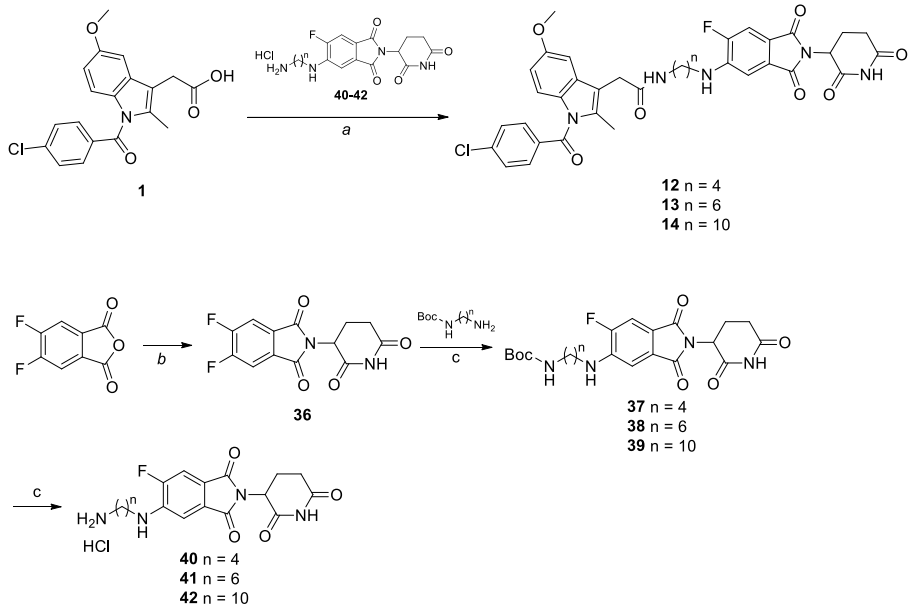

Scheme 5. Synthesis of PROTACs **12–14**. *Reagents and conditions*: (a) HATU, DIPEA, dry DMF, rt, 4 h; (b) AcOK, acetic acid, 110 °C, 4 h; (c) DIPEA, dry DMSO, 110 °C, 3 h; (d) HCl 4 N in dioxane, rt, 3 h.

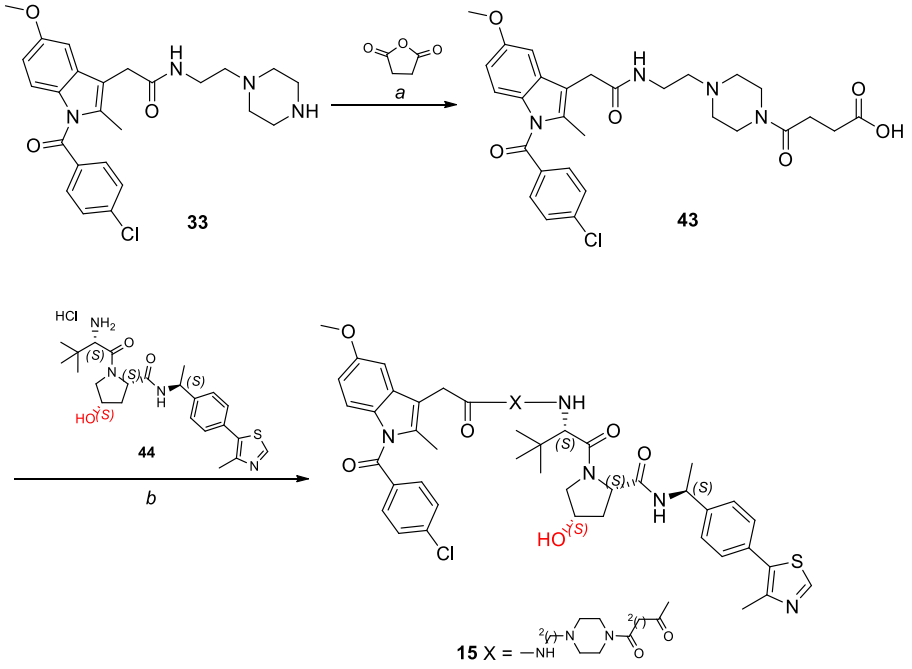

Scheme 6. Synthesis of compound **15**. *Reagents and conditions*: a) Et_3N, dry DCM, rt, 5 h; b) HATU, DIPEA, dry DMF, rt, 3 h.

PROTACs **6–11** as well as the epimer ligand **44** [73] used for the synthesis of negative controls **15** and **16** were prepared by applying a seven-steps column chromatography-free synthetic procedure (Scheme 8), similarly to the multi-gram scale synthetic process reported by Yan et al. for VH032 ligand [74]. In particular, (*S*)-1-(4-bromophenyl) ethanamine was initially *N*-Boc protected to furnish compound **47**, which was then coupled with 4-methylthiazole through a Pd (OAc)-catalyzed Heck reaction to give derivative **48**. The successive *N*-Boc deprotection of **48** under acid condition led to intermediate **49**, which was then coupled by HATU-mediated amidation reaction using (2S,4R)- and (2*S*,4*S*) 1-(*tert*-butoxycarbonyl)-4-hydroxypyrrolidine-2-carboxylic acid to give derivatives **50** and **51**, respectively. Their subsequent *N*-Boc deprotection led to intermediates **52** and **53** which were successively coupled with (*S*)-2-((*tert*-butoxycarbonyl)amino)-3,3-dimethylbutanoic acid by HATU-mediated amidation reaction to afford intermediates **54** and **55**. Their final *N*-Boc deprotection gave the target ligand **17** and **44** with an overall yield of 60 % and 66 %, respectively.

2.3. Evaluation of anti-coronavirus activity

The antiviral activity of the newly synthesized PROTACs **6–14** was first evaluated by plaque reduction assays (PRA) in Vero E6 cells infected with SARS-CoV-2/NL/2020 and compared to the results

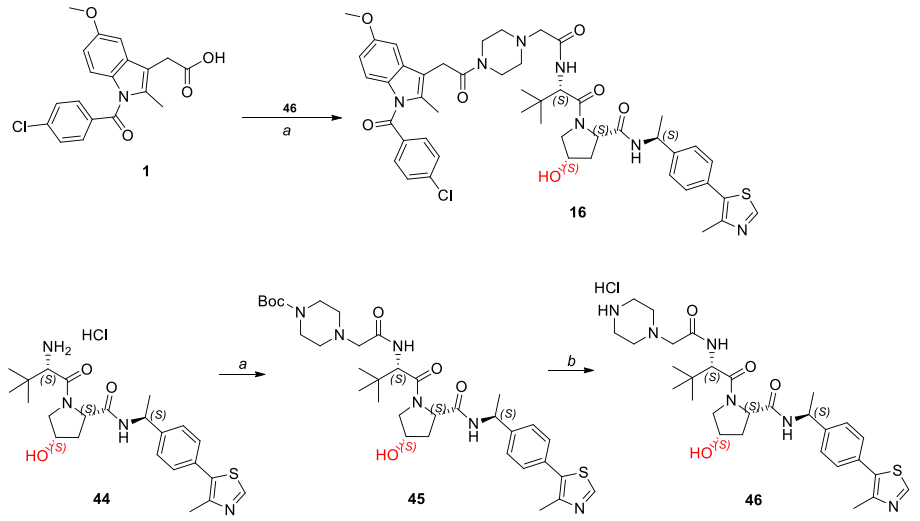

Scheme 7. Synthesis of compound **16**. *Reagents and conditions*: (a) appropriate *N*-Boc protected linker carboxylic acid derivative, HATU, DIPEA, dry DMF, rt, 2–3 h; b) HCl 4 N in dioxane, rt, 2–3 h.

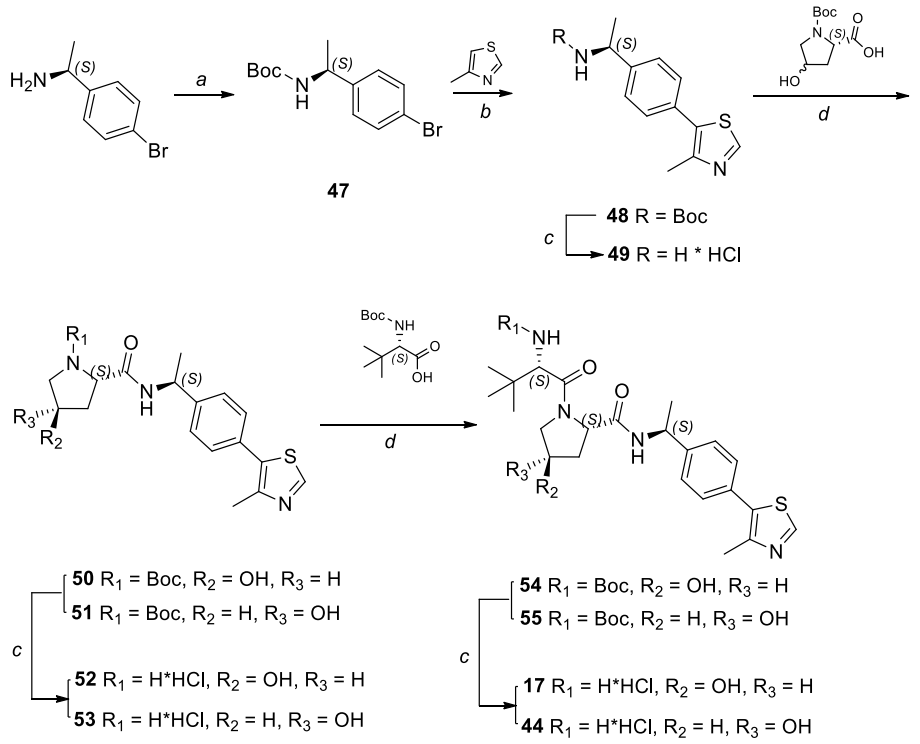

Scheme 8. Synthesis of VHL ligand **17** and inactive epimer ligand **44**. *Reagents and conditions*: a) Boc_2O, $NaHCO_3$, EA, H_2O, rt, 18 h; b) $Pd(OAc)_2$, AcOK, dry DMA, 130 °C, 4 h; c) HCl 4 N in dioxane, rt, 18 h; d) HATU, DIPEA, dry DMF, rt, 18 h.

previously obtained with PROTACs **3** and **5**. As reported in Table 1, among the newly synthesized VHL-recruiting PROTACs, with the exception of PROTAC **6**, the exploration of piperazine-containing linkers with atom linear linker length longer than 6 failed in improving the anti-SARS-CoV-2 activity of PROTACs **3** and **5**, regardless of the use of either aliphatic or PEGylated chains. In fact, only PROTAC **6** bearing the shortest piperazine acetyl linker inhibited SARS-CoV-2 replication (EC_{50} = 10.8 μM) at nontoxic concentrations (CC_{50} > 125 μM) more potently than the known SARS-CoV-2 M^{pro} inhibitor boceprevir (BOC, EC_{50} = 22.0 μM) used as a control compound. Analogously to PROTACs **3** and **5**, PROTAC **6** exhibited more potent antiviral activity against other HCoVs in human MRC-5 cells, such as the *β*-coronavirus HCoV-OC43 and the *α*-coronavirus HCoV-229E (EC_{50} = 1.6 μM and 6.5 μM, respectively).

2.4. Target investigation

We initially hypothesized that the anti-SARS-CoV-2 activity of the INM-based PROTACs **3**, **5** and **6** could be linked to the ability of INM to bind and inhibit PGES-2, a host protein reported to interact with HCoVs (SARS-CoV-2, SARS-CoV, and MERS-CoV) nsp7 protein [61,62]. To test this hypothesis, we investigated their ability to induce the degradation of PGES-2 by Western Blot analyses in both uninfected and virus-infected cells. As reported in Fig. 2a, none of the INM-based

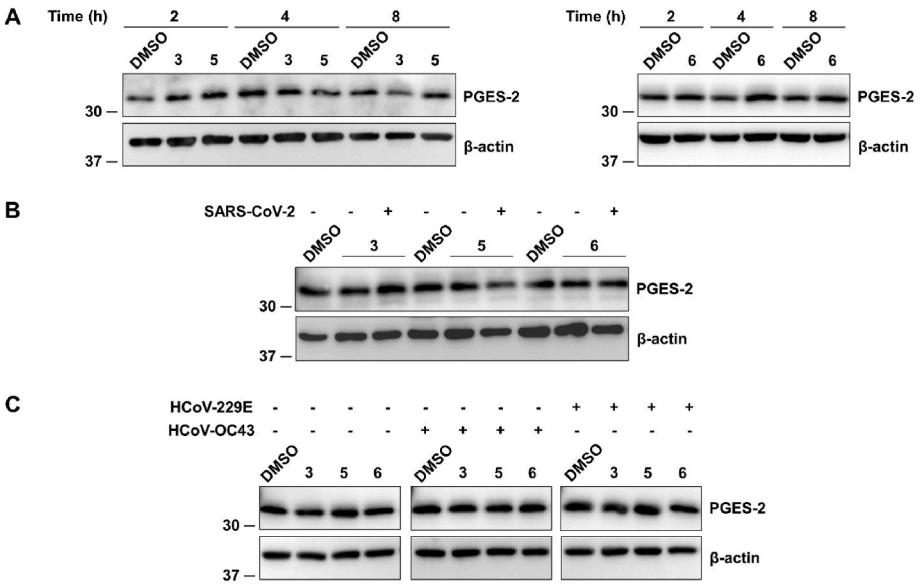

Fig. 2. Effects of PROTACs **3**, **5**, and **6** on PGES-2 levels in different uninfected and infected cell lines. A) Human 293T cells were treated with **3**, **5**, and **6** at 25 μM, or DMSO as a control and collected at the indicated times post-treatment. Whole cell lysates were analyzed by Western Blot with an antibody recognizing human PGES-2. B) Vero E6 cells were either left uninfected or infected with SARS-CoV-2 and then treated with **3**, **5**, and **6** at 25 μM, or DMSO as a control. Whole cell lysates were collected at 24 h post-infection and analyzed by Western Blot with an antibody recognizing human PGES-2. C) MRC-5 cells were either left uninfected or infected with HCoV-OC43 and HCoV-229E and then treated with **3**, **5**, and **6** at 25 μM, or DMSO as a control. Whole cell lysates were collected at 48 h post-infection and analyzed by Western Blot with an antibody recognizing human PGES-2. In all panels, β-actin was used as a loading control. Molecular masses in kDa are indicated on the left.

PROTACs showed the ability to induce the degradation of endogenous PGES-2 in human 293T cell line upon treatment for different times, suggesting that, differently from what initially hypothesized based on the literature [61,62], PGES-2 might not be the target of these PROTACs. To rule out the possible contribution of viral factors in the targeted degradation, we repeated the experiments in Vero E6 cells infected with SARS-CoV-2 and in MRC-5 cells infected with HCoVs-OC43 and -229E. However, also in cells infected with different CoVs and treated with different INM-based PROTACs, we did not detect relevant PGES-2 degradation even at longer times post-infection (Fig. 2b and c). Thus, we concluded that most likely the antiviral activity showed by PROTACs **3**, **5** and **6** is not dependent on PGES-2 degradation.

Considering these results, alternative hypotheses on the possible target were explored, based on other previously published results on INM, INM derivatives, and their antiviral activity against SARS-CoV-2. In particular, we recently identified INM as a potential SARS-CoV-2 M^{pro} inhibitor in a compound-repurposing approach based on pocket similarity search [75] using the BioGPS software [76]. However, in the subsequent biological evaluation, INM did not show significant inhibitory effects on M^{pro} catalytic activity *in vitro* under the tested experimental conditions, and displayed only weak activity on SARS-CoV-2 replication in infected cells [75]. Based on these results, at that time we did not progress further with INM. Later, we reasoned that one of the advantages of antiviral PROTACs design is the possibility of using ligands/binders with none or weak inhibitory effect as warheads. Thus, taking into account the computational outcomes, we decided that it was worth to investigate whether INM-based PROTACs could mediate M^{pro} degradation. For this reason, the SARS-CoV-2 M^{pro} degradation activity of PROTACs **3**, **5**, and **6** was evaluated in transfected 293T cells by Western Blot (Fig. 3). In these assays, the plasmid used for transfection allows the detection of the proteolytic cleavage of a FLAG-nsp4-M^{pro} fusion protein over-expressed in 293T cells and the release of an authentic M^{pro} protein. In the absence of M^{pro} inhibition, the expression of FLAG-nsp4-M^{pro} results in the cleavage of M^{pro} from the FLAG-nsp4

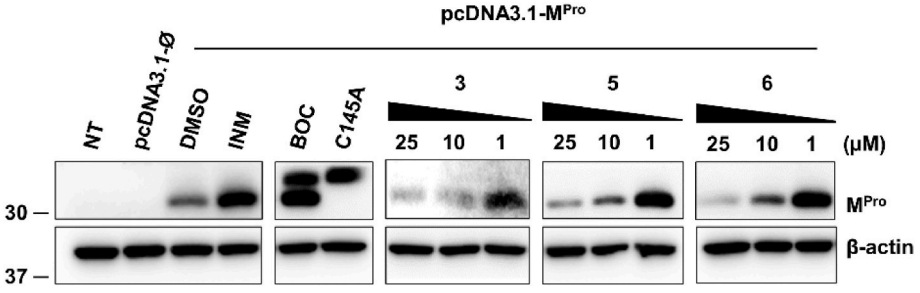

Fig. 3. Concentration-dependent degradation of SARS-CoV-2 M^{pro} in transfected 293T cells upon treatment with PROTACs **3**, **5**, and **6** for 24 h. Human 293T cells were transfected to overexpress either SARS-CoV-2 nsp4-M^{pro} fusion protein or its catalytically inactive mutant form (C145A). The expression of SARS-CoV-2 M^{pro} in either DMSO- or INM-treated cells resulted in the cleavage of M^{pro} and in the release of an authentic M^{pro} protein (with a molecular mass of ~34 kDa), which was not detected when the inactive mutant C145A (with a molecular mass of ~52 kDa) was expressed. Non-transfected 293T cells (NT), cells transfected with the empty plasmid, and transfected cells treated with DMSO or 100 μM boceprevir (BOC) were included as controls. The effects of the treatment of transfected cells with different concentrations (from 25 to 1 μM) of PROTACs **3**, **5**, and **6** is shown in the right panels. Whole cell lysates obtained from cells collected at 24 h post-transfection were analyzed by Western Blot with an antibody recognizing SARS-CoV-2 M^{pro}. β-actin was used as a loading control. Molecular masses in kDa are indicated on the left.

tag (thanks to a cleavage recognition site placed between the two proteins), producing a band with a molecular mass of ~34 kDa (Fig. 3, see DMSO-treated sample). In contrast, in cells treated with the M^{pro} inhibitor boceprevir or transfected with a plasmid expressing a catalytic inactive mutant of M^{pro}, i.e., C145A, an additional upper band is detected (Fig. 3). As reported in Fig. 3, upon treatment with PROTACs **3**, **5**, and **6** for 24 h of transfected 293T cells, wherein M^{pro} is overexpressed, we detected a concentration-dependent degradation of SARS-CoV-2 M^{pro}. Importantly, treatment of transfected cells with either INM or PROTACs **3**, **5**, and **6** did not produce two forms of M^{pro}, indicating that these compounds do not affect M^{pro} catalytic activity. This was also reconfirmed by testing them against M^{pro} *in vitro* in a FRET-based assay (Supplementary Table S1). For PROTACs **5** and **6**, the DC_{50} values were determined as 18.1 μM and 7.3 μM, respectively. In particular, treatment with both PROTACs at 25 μM remarkably counteracted the overexpression of M^{pro} in transfected cells (67 % of degradation for **5** and 72 % for **6**, respectively). For PROTAC **3**, due to poorly reproducible degradation most probably related to solubility issue (see paragraph 2.9.1), we could not determine a reliable DC_{50}.

2.5. Study of the biophysical binding of INM and PROTACs *3, 5, and 6* to SARS-CoV-2 M^{pro}

The microscale thermophoresis (MST) technique was used to investigate the binding of INM and INM-based PROTACs **3**, **5**, and **6** to SARS-CoV-2 M^{pro}. The recombinant SARS-CoV-2 M^{pro} (nsp5) was labelled with a fluorescent dye (NT650-M^{pro}) and its stability and integrity were checked using thermal shift analysis (TSA) to confirm that protein stability was not compromised after the incubation time and that structural integrity was maintained during the labelling reaction (Supplementary Fig. S1). Initially, the interaction with M^{pro} was investigated for INM and boceprevir as a positive control (Fig. 4), by examining a constant concentration of protein with a scalar concentration of ligand. For both compounds, binding curves were generated (Fig. 4) and K_d values were derived (Table 2). Data displayed that boceprevir was able to induce a variation of the thermophoretic movement of the ligand-bound NT650-M^{pro} complex, generating a binding curve with a K_d of 8.37 ± 1.41 μM, confirming the reliability of used protocol [77]. A binding curve and a K_d value of 129.05 ± 24.94 μM was also measured for INM, thereby detecting and confirming, for the first time, a specific interaction between this molecule and SARS-CoV-2 M^{pro}.

Due to low solubility issue (see paragraph 2.9.1), for PROTACs **3**, **5**, and **6** single-point binding assays were carried out with MST to explore their interaction with NT650-M^{pro}. Specifically, each PROTAC was tested at a concentration of 50 μM, along with 50 μM BOC, which was

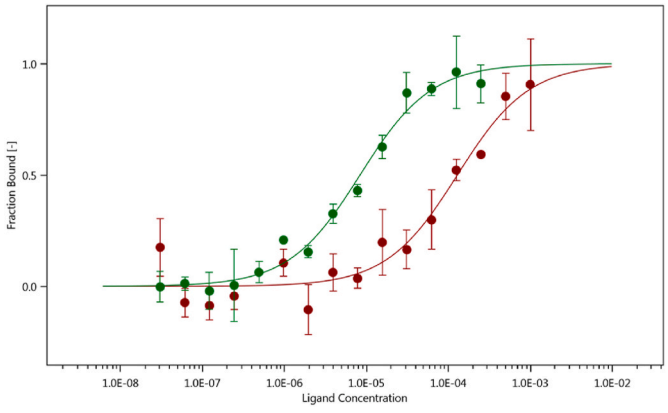

Fig. 4. Dose-response curves for the binding interaction of NT650-M^{pro} with BOC (green) and INM (red). The fraction bound is plotted against the ligand concentration. Graph represents the mean ± SD of n = 3 experiments in duplicate.

Table 2
Dissociation constant (K_d) and Signal to Noise (S/N) values obtained for boceprevir and indomethacin in MST binding assay.

Compd	K_d (μM)	S/N
BOC	8.37 ± 1.41	21.7
INM	129.05 ± 24.94	12.5

used as a positive control. Putative binders were defined as those molecules inducing a thermophoretic movement of the ligand-bound complex with a fluorescent signal (F_{norm}) outside the signal value and threefold standard deviations of the protein alone (vehicle, DMSO). Since vehicle F_{norm} value was 897.56 ± 0.16, a statistically significant thermophoretic shift was gained with F_{norm} values higher than 898.04 and lower than 897.08. Noteworthy, obtained results demonstrated that all three PROTACs induced a significant variation in M^{pro} thermophoretic motion, thus confirming their ability to bind M^{pro} (Supplemetary Fig. S2).

2.6. In-depth mechanism of action studies

Mechanistic studies were then performed to investigate the degradation mechanism of PROTACs **5** and **6**. Firstly, to confirm that the antiviral activity of PROTACs **5** and **6** was due to the VHL involvement, we synthesized and tested derivatives **S56** and **S57** (Supplementary Table S1), composed of only INM ligand coupled with the same linker moiety present in PROTACs **5** and **6**, respectively, but devoid of the VHL ligand. As reported in Supplementary Table S1, we did not detect any relevant activity for INM derivatives **S56** and **S57**, both *in vitro* and in infected cells, thus suggesting that the antiviral activity of PROTACs **5** and **6** most likely relies on a PROTAC-mediated mechanism rather than M^{pro} inhibitory activity.

Successively, we also synthesized compounds **15** and **16**, which are the corresponding negative controls of PROTACs **5** and **6**, bearing the *cis*-Hyp epimer of VHL ligand, unable to bind the VHL E3 ligase. As shown in Fig. 5a, compound **15** did not display any M^{pro} degradation activity, as expected, due to the inability to engage VHL E3 ligase to the ternary complex. Moreover, it did not inhibit SARS-CoV-2 replication in infected cells (Supplementary Table S2), thus confirming that the antiviral activity of PROTAC **5** relies on the VHL-mediated mechanism. Unfortunately, due to its high cytotoxicity (Supplementary Table S2), compound **16** could not be reliably tested in the M^{pro} degradation assays and in PRAs against SARS-CoV-2.

To further confirm that M^{pro} degradation by PROTACs **5** and **6** was indeed mediated through the engagement of the VHL E3 ligase, especially for PROTAC **6** whose negative control **16** resulted toxic, their degradation activity was also evaluated in the presence of the known VHL inhibitor VH298. As shown in Fig. 5b, the degradation effect of PROTACs **5** and **6** on M^{pro} was reversed upon VHL E3 ligase binding and inhibition.

As further investigation, we tested two compounds composed of only VHL ligand moiety and the same linker present in PROTACs **5** and **6**, respectively (**S58** and **S59** in Table S3). As reported in Supplementary Table S3, also in this case these compounds resulted unable to inhibit SARS-CoV-2 replication, thus confirming that the antiviral activity of PROTACs **5** and **6** relies on the PROTAC-mediated degradation and thus on the INM-mediated recruitment of target protein.

2.7. Computational modelling studies on ternary complexes mediated by PROTACs *5* and *6*

A previously used [27] *in house* developed algorithm was applied to elucidate the potential ternary complexes generated by PROTACs **5** and **6** with SARS-CoV-2 M^{pro} and VHL E3 ligase, and the best results for each complex are shown in Fig. 6. Details on model building are provided in the Experimental Section. Our models showed that the two ternary

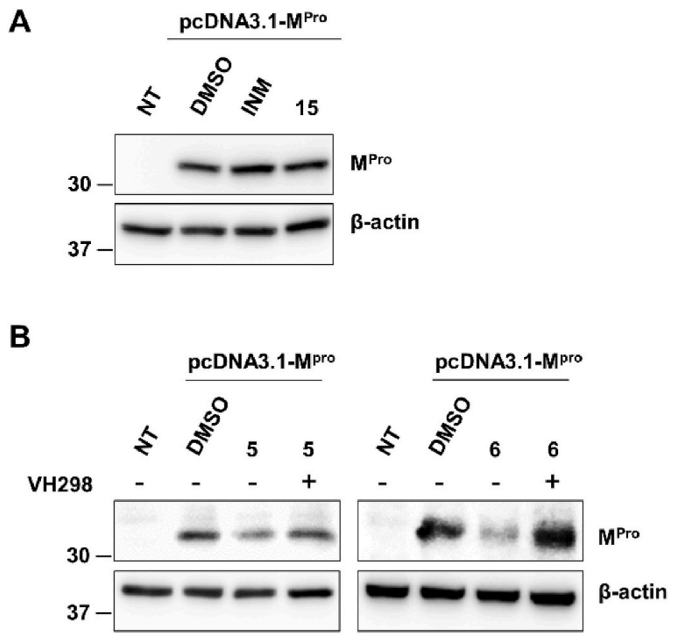

Fig. 5. Validation of the mechanism of PROTACs **5** and **6**. A) Human 293T cells were pre-treated with **15** at 25 μM and then transfected to overexpress SARS-CoV-2 M^{pro}. Non-trasfected (NT) cells and cells pre-treated with either DMSO or INM were included as controls. B) Human 293T cells were pre-treated with **5** and **6** at 25 μM in the absence or in the presence of 50 μM VHL inhibitor VH298 and then transfected to overexpress SARS-CoV-2 M^{pro}. NT cells and cells pre-treated with either DMSO were included as controls. In both panels, whole cell lysates obtained from cells collected at 24 h post-transfection were analyzed by Western Blot with an antibody recognizing SARS-CoV-2 M^{pro}. β-actin was used as a loading control. Molecular masses in kDa are indicated on the left.

complexes share a similar geometry, although the mutual orientation of the two proteins in each complex slightly changes (Fig. 6a and **c**). In more detail, in the ternary complex induced by PROTAC **5** (Fig. 6b) key interactions at the protein-protein interface between Q69 and Q19 of M^{pro} and R108 of the VHL E3 ligase were observed. In addition, the piperazine ring present in PROTAC **5** linker moiety, here modelled in its neutral form taking into account the associated pKa value (Table 2), is probably stabilized by both L141 of M^{pro} and R69 of VHL E3 ligase in terms of hydrophobic interactions, thus acting as a bridge. Concerning the ternary complex induced by PROTAC **6** (Fig. 6d), R69 in VHL E3 ligase was observed to directly interact with H172 of M^{pro}, and a similar polar interaction occurred between N67 in VHL E3 ligase and E169 in M^{pro}. In addition, a H-bond between E142 of M^{pro} and the NH- group of the amide bond used to attach VHL ligand to PROTAC **6** linker moiety was also observed. Although this is a preliminary computational analysis, that resulted even more complex due to the lack of x-ray crystallographic structures of indomethacin in complex with M^{pro}, these studies could be helpful in hypotheses generation and in shedding light on the key interactions (between POI-E3 or PROTAC with POI and E3) supporting the formation of productive ternary complexes mediated by PROTACs **5** and **6**.

2.8. Characterization of PROTAC *6* in human cells infected with SARS-CoV-2

We then evaluated the antiviral activity of the most promising PROTAC **6** in human lung cells (i.e., Calu-3) infected with SARS-CoV-2. As shown in Fig. 7a, PROTAC **6** exhibited very potent activity against SARS-CoV-2 in Calu-3 cells, with an EC_{50} in the nanomolar range (EC_{50} = 0.89 ± 0.20 μM), without showing cytotoxicity. These results supported that the exploitation of PROTAC technology on INM could lead to an increase in antiviral potency of 9- to 105-fold, depending on the cell line (Table 1 and Fig. 7a). The higher antiviral potency of PROTAC **6** in human cells (MRC-5 and Calu-3) with respect to that observed in Vero E6 cells might be related to differences in the expression of efflux transporters, which can affect the antiviral activity in Vero E6 cells [78], or to different expression levels of the VHL E3 ligase. Then, to further confirm the degradation activity in the context of infection, we evaluated the ability of PROTAC **6** to induce the degradation of virus-expressed M^{pro} in SARS-CoV-2 infected Calu-3 cells. As reported in Fig. 7b, PROTAC **6** induced a concentration-dependent degradation of SARS-CoV-2 M^{pro}, with a DC_{50} value of 1.34 μM, in keeping with the higher antiviral activity observed in Calu-3 cells and with the fact that, most likely, in the context of viral infection PROTAC **6** is more active than in transfected cells, wherein M^{pro} is over-expressed.

2.9. Evaluation of PROTACs solubility and chemical and metabolic stability

2.9.1. Focus on the modulation of solubility based on linker composition

To shed light on how the modifications made at the linker moiety of all VHL-recruiting PROTACs in our series (**3**, **5**, and **6–11**) may affect their physico-chemical properties, the kinetic solubility was experimentally determined (Table 3). Indeed, as recently demonstrated, the pK_a values and protonation state of piperazine moieties inserted in PROTACs' linkers heavily depend on the structural environment and neighbouring groups [66], and the protonation is expected to improve the solubility. Among the tested compounds, the kinetic solubility for four PROTACs (**3**, **6**, **7** and **8**) was under the limits of detection/quantification (Table 3). This is in line with the evidence that these three PROTACs are mostly in their neutral form, with a percentage of protonated form lower than 2 %. In addition, data suggest that increasing the distance of the protonable piperazine nitrogen atom from carbonyl group, and therefore increasing basicity as previously reported [66], is not always an efficient approach to increase solubility. Indeed, in aliphatic linkers the presence of the charge is counterbalanced by the increase in lipophilicity, and thus a gain in solubility is not observed, as in PROTAC **8**. Contrarily, in our series the presence of PEG-based linkers contributes synergically with a protonable piperazine to improve solubility, with PROTAC **11** resulting the most soluble one. Indeed, PEG units allowed achieving higher solubility, as in PROTAC **11**, as the result of a higher percentage of protonation state.

Unfortunately, the structural modifications enhancing the solubility of the final PROTACs resulted detrimental for the biological activity, in keeping with the fact that it is known that the length and flexibility of linker moiety is pivotal for the formation of functional ternary complexes and thus in influencing the activity of degraders.

2.9.2. Chemical stability studies on PROTACs *5* and *6*

For the most promising INM-based PROTACs **5** and **6**, the chemical stability was investigated in the same medium used for the cellular assays (Experimental section, paragraph 4.12). In this assay, PROTACs **5** and **6** (1 and 10 μM with 0.1 % DMSO) were incubated at 37 °C in DMEM (pH 7.4) and samples were collected at 0 and after 24 h. Each sample was then analyzed by LC-MS and, successively, raw data were processed by using MassChemSite (Molecular Discovery Ltd.) within the WebChembase platform [79,80] to automatically identify possible degradation products (Supplementary Fig. S3). Under these conditions, both the analyzed PROTACs showed a general good chemical stability in cellular medium (Fig. 8), with a relative area percentage of remaining PROTAC over 70 % at 24 h when assayed at 1 μM (Fig. 8). As suggested by automatic structure elucidation analyses through MassChemSite and WebChemBase, a recurrent chemical degradation reaction is due to amide hydrolysis between indole ring and the *p*-chloro benzoyl ring at the INM moiety (**DP1** and **DP2**, Fig. S3).

2.9.3. Metabolic stability studies on PROTACs 5 and 6

For PROTACs **5** and **6** the metabolic stability in human liver

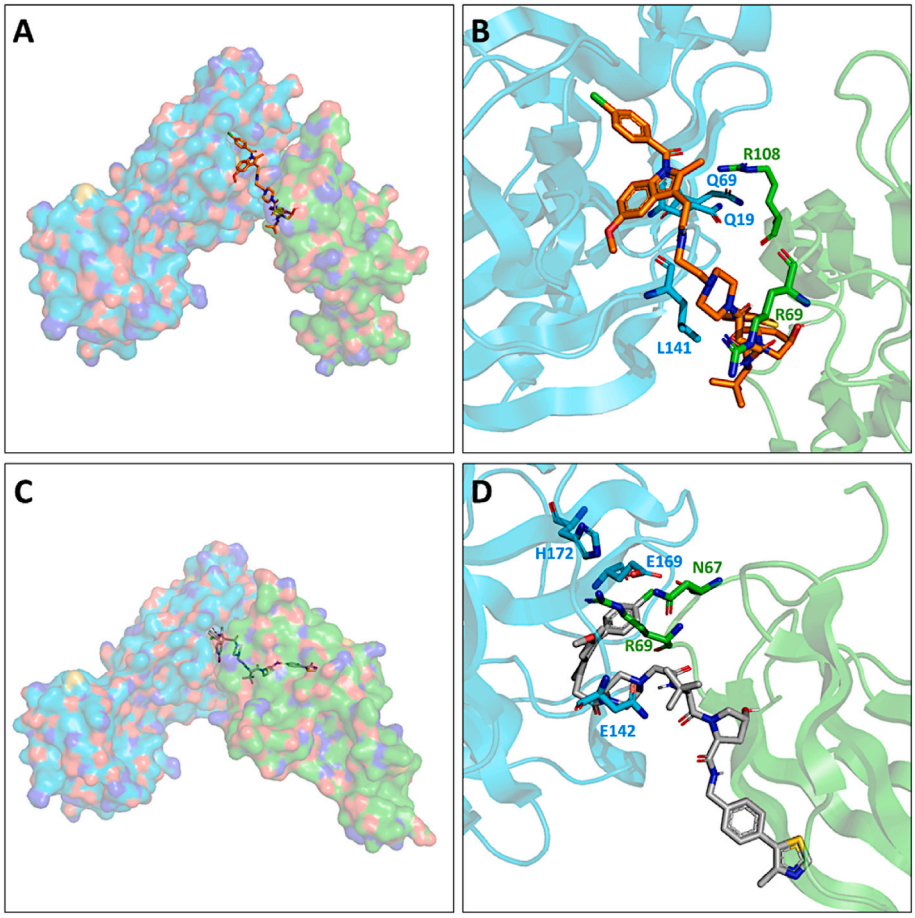

Fig. 6. Model of SARS-CoV-2 M^{pro}/PROTAC **5**/VHL and M^{pro}/PROTAC **6**/VHL ternary complexes. A-B) Overall view of the generated ternary complex and observed key interactions for SARS-CoV-2 M^{pro}/PROTAC **5**/VHL, respectively. C-D) Overall view of the generated ternary complex and observed key interactions for SARS-CoV-2 M^{pro}/PROTAC **6**/VHL, respectively. SARS-CoV-2 M^{pro} and VHL E3 ligase are depicted in light-blue and green, respectively.

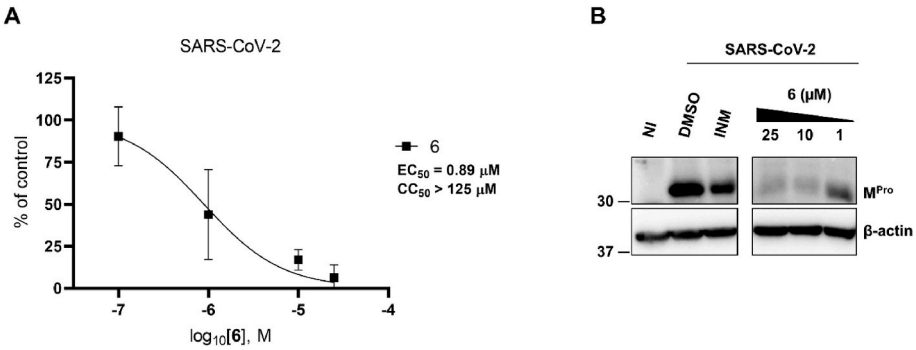

Fig. 7. Activity of PROTAC **6** in human Calu-3 cells infected with SARS-CoV-2. A) Antiviral activity of PROTAC **6** in human lung Calu-3 cells infected with SARS-CoV-2 and treated with different concentrations of **6**. At 36 h p.i., supernatants were collected and titrated onto fresh Vero E6 cell monolayers. Graph represents the mean ± SD of n = 3 experiments in duplicate. The CC_{50} value was obtained by MTT assays in Calu-3 cells at 72 h. B) Concentration-dependent degradation of M^{pro} in SARS-CoV-2-infected cells upon treatment with PROTAC **6**. Calu-3 cells were infected with SARS-CoV-2 and treated with different concentrations of **6** (from 25 to 1 μM) for 48 h. Non-infected Calu-3 cells (NI) and infected cells treated with DMSO or 25 μM indomethacin (INM) were included as controls. Whole cell lysates were analyzed by Western Blot with an antibody recognizing SARS-CoV-2 M^{pro}. β-actin was used as a loading control. Molecular masses in kDa are indicated on the left.

microsomes (HLM) was also studied by monitoring the percentage of unmodified substrate and the formation of metabolites over a period of 60 min incubation (time points: 0, 5, 15, 30 and 60 min) (Fig. 9). Samples were analyzed by LC-MS/MS and the raw data were analyzed by using Mass-MetaSite (Molecular Discovery Ltd.) [81–83] and Web-Metabase (Molecular Discovery Ltd.) [84,85] software for automatic metabolite identification and structure elucidation as well as for kinetic analysis. Overall, both PROTACs demonstrated good metabolic stability, with half-life >60 min. Although the metabolite identification does not provide quantitative data due to the lack of standards, it resulted evident that the nature of the linker has a strong impact on detected metabolites. For instance, the most rigid and short linker in PROTAC **6** did not show metabolic liability, in agreement with our previous findings [65], while the *N*-dealkylation reaction) occurred when flexibility is increased, as in PROTAC **5**. Additional metabolic transformations ascribed to aliphatic hydroxylation reactions were observed for the linker in PROTAC **5**.

Table 3
Experimental kinetic solubility and pKa values of PROTACs **3**, **5**, and **6–11**.

Compd	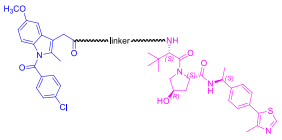 Linker	Atom linker length	Kinetic Solubility in Universal Buffer[a] (μM)	Most basic pKa value	% protonation at pH 7.5[d]
3	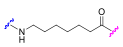	8	<LOD	–	NI: 99.7[c]
5	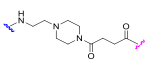	11	6 ± 1	5.88 ± 0.13[b]	NI: 97.66 P: 2.34
6		6	<LOD	5.36 ± 0.19[b]	NI: 99.28 P: 0.72
7		7	<LOQ	5.73 ± 0.04[b]	NI: 98.33 P: 1.77
8	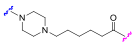	10	<LOD	7.00 ± 0.61[c]	NI: 75.9[c] P: 23.9[c]
9	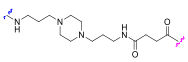	16	9.4 ± 0.3	7.81 ± 0.04[b]	NI: 32.86 P: 67.11; DP:0.02
10	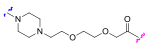	12	7.7 ± 0.8	6.27 ± 0.04[b]	NI: 94.44 P: 5.56
11	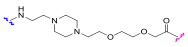	15	26 ± 2	7.47 ± 0.09[b]	NI: 51.72 P: 48.27; DP: 0.002

[a] Mean ± standard deviation of n = 3 experiments; LOD (limit of detection); LOQ (limit of quantification).
[b] Experimental measurements of pKa values performed by using the SiriusT3 platform, applying a potentiometric acid–base titration. Mean ± standard deviation of n = 3 experiments. Data reported in Ref. [66].
[c] pKa values predicted with Moka 4.0.12 (Molecular Discovery Ltd.) and in line with what previously measured in Ref. [66].
[d] NI: not-ionized state; P: single protonation state, DP: double protonation state.

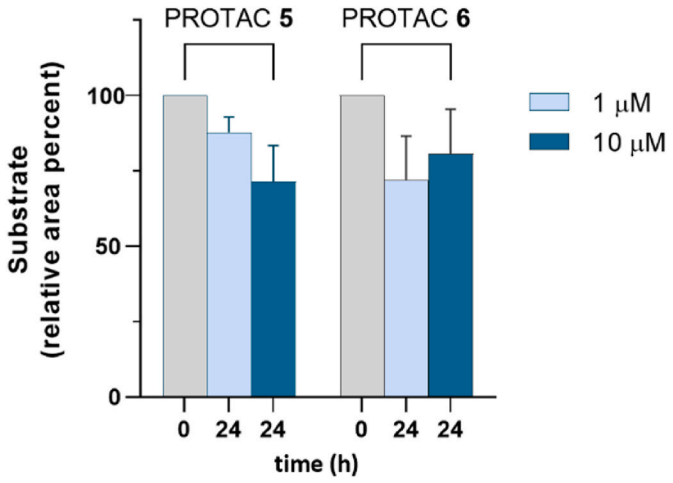

Fig. 8. Chemical stability of PROTACs **5** and **6** in the medium used in the cell-based assays. DMSO stock solutions of PROTACs **5** and **6** were mixed with DMEM containing 10 % of FBS and 100 U/mL penicillin and 100 μg/mL streptomycin and incubated at 37 °C up to 24 h. At each time point (0 and 24 h), aliquots were analyzed by LC-MS and normalized to labetalol, used as an internal standard. Data reported in the graph represent the mean ± SD from n = 2 experiments.

Intriguingly, a series of metabolites originated from the indomethacin moiety for PROTAC **6**, with liabilities at the amide bond and the methyl group. None of these reactions were observed in PROTAC **5** and, since reactivity of the indomethacin moiety is likely to be the same, we hypothesize that the linker in PROTAC **5** could hamper an efficient exposition of the warhead (Fig. 9).

3. Conclusions

Despite the exceptionally rising of attention reached by PROTAC technology in drug development in the last years, its evolution in the antiviral field is still limited. The number of reported antiviral PROTACs is extremely low if compared to those developed for other diseases, such as cancers, immune disorders, and neurodegenerative diseases. Nevertheless, the results obtained with the few antiviral PROTAC-based degraders reported so far, clearly confirm that they could be used to contrast different viral infections (i.e., hepatitis C virus, coronaviruses, and influenza virus) and could effectively overcome the emergence of mutant viral strains compared to small-molecules inhibitors.

Starting from the non-steroidal anti-inflammatory drug indomethacin and exploiting PROTAC technology, we recently identified INM-based PROTACs **3** and **5** endowed with broad-spectrum anti-CoV activity [27]. In this study, with the aim of further investigating this promising class of PROTACs, we enlarged the panel of VHL-recruiting PROTACs by exploring the piperazine-containing linker, thus leading to the identification of PROTAC **6**. Indeed, the biological evaluation demonstrated that PROTAC **6**, analogously to PROTACs **3** and **5**, exhibited broad-spectrum antiviral activity against CoVs, including SARS-CoV-2 (EC_{50} = 10.8 μM) and two different endemic human CoVs (EC_{50} = 1.6 and 6.5 μM against HCoV-OC43 and HCoV-229E, respectively) at nontoxic concentrations. Its antiviral activity against SARS-CoV-2 was also confirmed in a human cell line with an EC_{50} in the nanomolar range (EC_{50} = 890 nM). No active degraders were instead generated by coupling INM with a CRBN recruiter.

To shed light on the mechanism of action of PROTACs **3**, **5**, and **6** and on their target, the first investigation was focused on the evaluation of

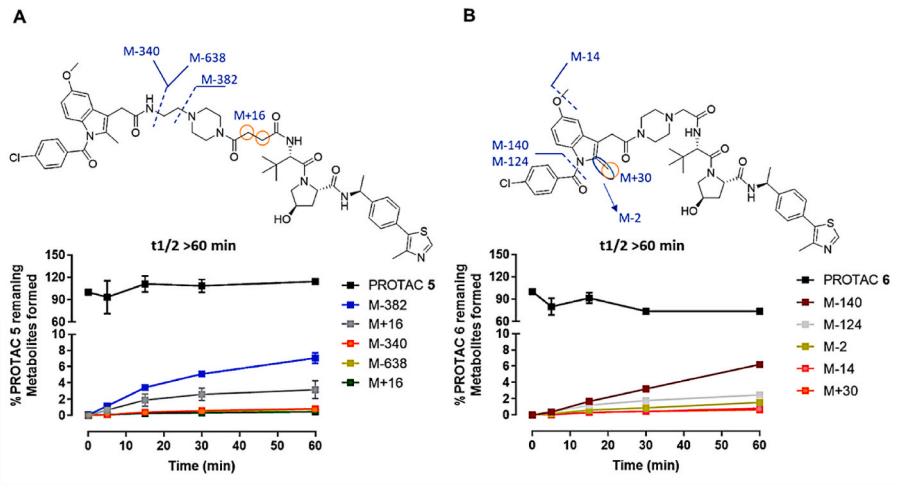

Fig. 9. Metabolic stability in HLM of PROTACs **5** and **6** over a 60-min incubation. Chemical structures of PROTACs **5** (A) and **6** (B), respectively, with the liability points (soft spots) related to the sites of metabolism are depicted on the top of each panel. For each compound, observed behaviour for substrate metabolic degradation is shown in black while formation of metabolites, whose names are expressed referring to the mass variation compared to the one of substrate, is shown in coloured lines. Data reported in the graph represent the mean ± SD from n = 3 experiments. The half-life values associated to each compound and expressed in minutes are reported in bold.

their ability to degrade human PGES-2. Indeed, INM is an inhibitor of PGES-2 [63], a host protein proposed by Gordon et al. as a potential pan-CoV antiviral target due to its interaction with SARS-CoV-2 nsp7 protein. However, Western blot analyses in both uninfected and virus-infected cells showed that INM-PROTACs do not degrade PGES-2 as initially hypothesized, but have the ability to induce the degradation of SARS-CoV-2 M^{pro}. In-depth studies on the degradation mechanism confirmed that the anti-SARS-CoV-2 activity and M^{pro} degradation efficacy of PROTACs **5** and **6** depend on both VHL E3 ligase engagement and the INM-mediated recruitment of target protein. To note, for the first time binding experiments with MST confirmed the ability of INM to bind to SARS-CoV-2 M^{pro}, although with a weak binding affinity. PROTACs **5** and **6** were also found to bind to M^{pro} at 50 μM, but solubility issue hampered their complete characterization.

Moreover, molecular modelling studies highlighted the key interactions at the protein-protein interface as well as at the PROTAC-protein interface providing a model of the potential ternary complexes generated by PROTACs **5** and **6** with M^{pro} and VHL E3 ligase.

Finally, since physico-chemical and ADME properties remain the under-investigated and challenging tasks for PROTACs in clinical development, solubility as well as chemical and metabolic stability of PROTACs **5** and **6** have been investigated. Although further optimization will be required in order to improve their aqueous solubility, both PROTACs exhibited good chemical and metabolic stability, and the pivotal effect of the linker in soft spots number and position has been further highlighted.

During the revision of the present manuscript two different works reporting SARS-CoV-2 M^{pro} degraders have been also published [86,87]. In the first one, M^{pro} degraders reported in two different patents have been reviewed, while in the second one, the characterization of one PROTAC inducing M^{pro} degradation has been described. In all cases, covalent inhibitors of M^{pro} have been used for PROTACs design leading to compounds with good degradation efficacy (<100 nM and 621 nM, respectively) and potent anti-SARS-CoV-2 activity, when evaluated. To our knowledge, our study is the first report of anti-CoVs PROTACs able to induce the degradation of the POI without inhibiting its enzymatic activity and that are able to induce the degradation of M^{pro} also in the context of viral infection.

In conclusion, herein we identified and presented the mechanism of action of the first class of INM-based SARS-CoV-2 M^{pro} degraders endowed with pan-CoVs inhibitory activity thanks to the engagement of VHL E3 ligase. To note, for the first time it has been confirmed that PROTAC technology applied to a weak affinity POI binder may result in potent antiviral degraders. The experimental elucidation of the ternary complex formation will be useful in the future to guide further optimization studies.

4. Experimental section

4.1. General synthetic procedures

Unless otherwise noted, starting materials, reagents, and solvents were purchased from commercial suppliers and were used without further purification.

The synthesis of PROTACs **6–11** was already described by Desantis et al. [66]. The synthesis of intermediates **18–21** was already described by Goracci et al. [65], while the synthesis of intermediates **26–35** was reported by Desantis et al. [66]. Compounds **S56** and **S57** were prepared as already described by Desantis et al. [66], compounds **S58** as described by Desantis et *al.* [27], while **S59** as described by Goracci et al. [65].

Reactions were routinely monitored by thin-layer chromatography (TLC) performed on silica gel 60 F254 (layer 0.2 mm) pre-coated aluminium foil (with fluorescent indicator UV254) (Sigma-Aldrich).

Developed plates were air-dried and visualized by UV detector (λ: 254/365 nm) and/or by staining and warming with potassium permanganate or ninhydrin. Flash column chromatography was performed on Merck silica gel 60 (mesh 230–400). Automated flash chromatography was performed using Biotage® Selekt with Sfär Silica HC Duo 5g or 10g cartridges. ^{1}H NMR and ^{13}C NMR spectra were recorded at room temperature at 400 and 101 MHz, respectively, on a Bruker Avance 400 spectrometer in the indicated solvent by using residual solvent peak as an internal standard. Chemical shifts are reported in ppm (δ) and the coupling constants (J) are given in Hertz (Hz). Peak multiplicities are abbreviated as follows: s (singlet), bs (broad singlet), d (doublet), dd (double doublet), t (triplet), dt (double triplet), q (quartet), p (pentet), and m (multiplet). High-Resolution Mass Spectroscopy (HRMS) analyses were carried out on Agilent Technologies 6540 UHD Accurate Mass Q-TOF LC-MS system. The purity of all synthesized compounds was confirmed to be >95 % by UPLC-MS. The analyses were carried out according to the method listed below. The mobile phase was a mixture of water (solvent A) and acetonitrile (solvent B), both containing formic acid at 0.1 %. Method: Acquity UPLC BEH C18 1.7 μm (C18, 150 × 2.1

mm) column at 40 °C using a flow rate of 0.65 mL/min in a 10 min gradient elution. Gradient elution was as follows: 99.5:0.5 (A/B) to 5:95 (A/B) over 8 min, 5:95 (A/B) for 2 min, and then reversion back to 99.5:0.5 (A/B) over 0.1 min. The UV detection is an averaged signal from a wavelength of 190 nm–640 nm and mass spectra are recorded on a mass spectrometer using positive mode electro spray ionization.

4.1.1. General procedure A: HATU-mediated amidation

Under nitrogen atmosphere, to a stirred solution of the appropriate carboxylic acid (1.0 equiv), suitable amine (1.0 equiv) and DIPEA (4.0 equiv) in dry DMF was added HATU (1.25 eq) and the reaction mixture was stirred at room temperature. The mixture was poured in ice-water yielding a precipitate collected by filtration. When no precipitate formed, the mixture was extracted with EA (x3) and the reunited organic phases were washed with water (x3), brine (x3), dried over Na_2SO_4, and evaporated to dryness. The crude was purified as described below.

4.1.2. General procedure B: amine Boc-deprotection

A solution of 4.0 N HCl in dioxane was added to the appropriate Boc-protected amine and the resulting solution was stirred at room temperature for 2–3 h. The solvent was evaporated to dryness and the residue was triturated with DEE, collected by filtration, and dried *in vacuo*.

4.2. Synthesis of PROTAC 8

(2*S*,4*R*)-1-((*S*)-2-(6-(4-(2-(1-(4-Chlorobenzoyl)-5-methoxy-2-methyl-1*H*-indol-3-yl)acetyl)piperazin-1-yl)hexanamido)-3,3-dimethylbutanoyl)-4-hydroxy-*N*-((*S*)-1-(4-(4-methylthiazol-5-yl)phenyl) ethyl)pyrrolidine-2-carboxamide (8).

General Procedure A (3 h) was followed by using **1** (0.024 g, 0.066 mmol) and **25** (0.044 g, 0.066 mmol) to afford the titled compound as a white powder (0.012 g, 19 % yield) after purification by flash column chromatography on SiO_2 (DCM/Acetone/MeOH, 82:10:8). ^{1}H NMR (400 MHz, $CDCl_3$) δ 8.67 (s, 1H), 7.65 (d, J = 8.3 Hz, 2H), 7.55–7.31 (m, 7H), 7.02–6.91 (m, 1H), 6.82 (d, J = 9.0 Hz, 1H), 6.65 (dd, J = 9.0, 1.9 Hz, 1H), 6.15 (d, J = 8.3 Hz, 1H), 5.14–5.03 (m, 1H), 4.72 (t, J = 7.9 Hz, 1H), 4.60–4.46 (m, 2H), 4.09 (d, J = 11.3 Hz, 1H), 3.81 (s, 3H), 3.77–3.65 (m, 4H), 3.64–3.53 (m, 3H), 2.63–2.30 (m, 13H), 2.24–2.16 (m, 2H), 2.11–2.01 (m, 1H), 1.71–1.55 (m, 2H), 1.54–1.38 (m, 5H), 1.35–1.26 (m, 2H), 1.04 (s, 9H); ^{13}C NMR (101 MHz, $CDCl_3$) δ 173.52, 172.17, 169.51, 168.63, 168.27, 156.00, 150.29, 148.51, 143.12, 139.31, 135.19, 133.85, 131.55, 131.21 (2C), 130.91, 130.84, 130.63, 129.58 (2C), 129.13 (2C), 126.42 (2C), 114.89, 113.19, 111.52, 101.54, 69.96, 58.33, 57.99, 57.57, 56.70, 55.76, 53.02, 52.61, 48.87, 45.45, 41.60, 36.15, 35.43, 34.95, 30.23, 26.83, 26.52 (3C), 25.79, 25.09, 22.27, 16.11, 13.47. HRMS *m/z* $[M+Na]^+$ calcd for $C_{52}H_{64}ClN_7O_7S$ 988.41742, found 988.42044. UPLC retention time: 5.063 min.

4.2.1. 6-(4-(Tert-butoxycarbonyl)piperazin-1-yl)hexanoic acid (23)

To the solution of **22** [88] (0.150 g, 0.477 mmol) in THF (2.0 mL) at 0 °C was added the solution of LiOH monohydrate (0.060 g, 1.431 mmol) in H_2O (1.0 mL). The reaction was stirred at room temperature for 3 h. Then, the organic solvent was evaporated under reduced pressure and the mixture was extracted with EA (x3); the reunited organic phases were washed with brine (x1), dried over Na_2SO_4, and evaporated to dryness to give a colourless oil (0.049 g, 34 % yield). ^{1}H NMR (400 MHz, $CDCl_3$) δ 9.09 (bs, 1H), 3.58–3.46 (m, 4H), 2.75–2.60 (m, 4H), 2.60–2.48 (m, 2H), 2.30–2.19 (m, 2H), 1.65–1.51 (m, 4H), 1.43 (s, 9H), 1.38–1.28 (m, 2H).

4.2.2. Tert-butyl 4-(6-(((S)-1-((2S,4R)-4-hydroxy-2-(((S)-1-(4-(4-methylthiazol-5-yl)phenyl)ethyl)carbamoyl)pyrrolidin-1-yl)-3,3-dimethyl-1-oxobutan-2-yl)amino)-6-oxohexyl)piperazine-1-carboxylate (24)

General Procedure A (3 h) was followed by using **23** (0.048 g, 0.160 mmol) and **17** (0.077 g, 0.160 mmol) to afford the titled compound as a colourless oil (0.048 g, 41 % yield) after purification by automated flash chromatography on SiO_2 cartridge (DCM/MeOH, 95:5). ^{1}H NMR (400 MHz, $CDCl_3$) δ 8.66 (s, 1H), 7.40–7.30 (m, 5H), 6.62–6.53 (m, 1H), 5.12–5.00 (m, 1H), 4.66 (t, J = 8.3 Hz, 1H), 4.55–4.44 (m, 2H), 4.04 (d, J = 10.9 Hz, 1H), 3.64–3.52 (m, 5H), 2.84–2.59 (m, 6H), 2.51 (s, 3H), 2.37–2.27 (m, 1H), 2.27–2.07 (m, 3H), 1.64–1.53 (m, 4H), 1.49–1.40 (m, 12H), 1.35–1.24 (m, 2H), 1.03 (s, 9H).

4.2.3. (2S,4R)-1-((S)-3,3-Dimethyl-2-(6-(piperazin-1-yl)hexanamido) butanoyl)-4-hydroxy-N-((S)-1-(4-(4-methylthiazol-5-yl)phenyl)ethyl) pyrrolidine-2-carboxamide dihydrochloride (25)

General Procedure B (3 h) was followed by using **24** (0.045 g, 0.062 mmol) and 4.0 N HCl in dioxane (0.45 mL) to afford the titled compound as a white solid (0.038 g, 93 % yield). ^{1}H NMR (400 MHz, MeOD) δ 9.83 (d, J = 2.0 Hz, 1H), 7.58–7.47 (m, 4H), 5.06–4.98 (m, 1H), 4.62–4.57 (m, 1H), 4.47–4.40 (m, 1H), 3.92–3.45 (m, 11H), 3.30–3.23 (m, 2H), 2.60 (s, 3H), 2.34 (t, J = 7.3 Hz, 2H), 2.27–2.19 (m, 1H), 1.99–1.89 (m, 1H), 1.88–1.78 (m, 2H), 1.73–1.64 (m, 2H), 1.52 (d, J = 7.0 Hz, 3H), 1.48–1.38 (m, 2H), 1.05 (s, 9H).

4.3. Synthesis of PROTACs 12-14

4.3.1. 2-(1-(4-chlorobenzoyl)-5-methoxy-2-methyl-1H-indol-3-yl)-N-(4-((2-(2,6-dioxopiperidin-3-yl)-6-fluoro-1,3-dioxoisoindolin-5-yl)amino) butyl)acetamide (12)

General Procedure A (4 h) was followed by using **1** (0.028 g, 0.075 mmol) and **40** (0.030 g, 0.075 mmol) to afford the titled compound as yellow solid (0.020 g, 38 % yield) after purification by automated flash column chromatography on SiO_2 cartridge (DCM:MeOH, 98:2) followed by preparative TLC eluting with DCM:MeOH 97:3. ^{1}H NMR (400 MHz, $CDCl_3$) δ 8.11 (bs, 1H), 7.69–7.63 (m, 2H), 7.52–7.45 (m, 2H), 7.37 (d, J = 9.8 Hz, 1H), 7.01 (d, J = 7.1 Hz, 1H), 6.88 (d, J = 2.5 Hz, 1H), 6.84 (d, J = 9.0 Hz, 1H), 6.69 (dd, J = 9.1, 2.5 Hz, 1H), 5.68 (t, J = 6.1 Hz, 1H), 4.95–4.87 (m, 1H), 4.79 (bs, 1H), 3.80 (s, 3H), 3.66 (s, 2H), 3.32–3.17 (m, 4H), 2.92–2.67 (m, 3H), 2.39 (s, 3H), 2.15–2.08 (m, 1H), 1.60–1.51 (m, 4H). ^{13}C NMR (101 MHz, $CDCl_3$) δ 170.87, 170.11, 168.37, 168.23, 167.34, 166.81 (d, J = 2.9 Hz), 156.26, 153.62 (d, J = 248.4 Hz), 142.47 (d, J = 12.8 Hz), 139.73, 136.45, 133.43, 131.24 (2C), 130.94, 130.21, 130.08 (d, J = 2.3 Hz), 129.26 (2C), 118.37 (d, J = 8.7 Hz), 115.13, 112.71, 112.19, 110.05 (d, J = 22.4 Hz), 105.36 (d, J = 5.3 Hz), 101.00, 55.81, 49.27, 42.84, 39.00, 32.26, 31.45, 27.27, 25.97, 22.74, 13.24. HRMS *m/z* [M+Na]+ calcd for $C_{36}H_{33}ClFN_5O_7$ 724.19502, found 724.19524. UPLC retention time: 5.742 min.

4.3.2. 2-(1-(4-chlorobenzoyl)-5-methoxy-2-methyl-1H-indol-3-yl)-N-(6-((2-(2,6-dioxopiperidin-3-yl)-6-fluoro-1,3-dioxoisoindolin-5-yl)amino) hexyl)acetamide (13)

General Procedure A (4 h) was followed by using **1** (0.030 g, 0.084 mmol) and **41** (0.036 g, 0.084 mmol) to afford the titled compound as yellow solid (0.021 g, 34 % yield) after purification by automated flash column chromatography on SiO_2 cartridge (DCM:MeOH, 98:2) followed by preparative TLC eluting with DCM:Acetone:MeOH 89:10:1. ^{1}H NMR (400 MHz, $CDCl_3$) δ 8.03 (s, 1H), 7.66 (d, J = 8.4 Hz, 2H), 7.48 (d, J = 8.4 Hz, 2H), 7.39 (d, J = 9.9 Hz, 1H), 7.03 (d, J = 7.1 Hz, 1H), 6.94–6.78 (m, 2H), 6.69 (dd, J = 9.0, 2.0 Hz, 1H), 5.69–5.58 (m, 1H), 4.97–4.86 (m, 1H), 4.70 (bs, 1H), 3.81 (s, 3H), 3.64 (s, 2H), 3.30–3.07 (m, 4H), 2.93–2.67 (m, 3H), 2.39 (s, 3H), 2.17–2.07 (m, 1H), 1.67–1.54 (m, 4H), 1.47–1.31 (m, 4H), 1.29–1.19 (m, 2H).^{13}C NMR (101 MHz, $CDCl_3$) δ 170.83, 169.84, 168.39, 168.16, 167.42, 166.85 (d, J = 2.9 Hz), 153.64 (d, J = 248.0 Hz), 152.41, 142.61 (d, J = 12.7 Hz), 139.70, 136.36, 133.49, 131.24 (2C), 130.93, 130.29, 130.13 (d, J = 2.3 Hz), 129.26 (2C), 118.25 (d, J = 8.8 Hz), 115.11, 112.91, 112.30, 110.05 (d, J = 22.4 Hz), 105.44 (d, J = 5.4 Hz), 100.91, 55.79, 49.28, 42.97, 39.36, 32.30, 31.45, 29.46, 28.75, 26.36, 26.32, 22.75, 13.25. HRMS *m/z* [M+Na]+ calcd for $C_{38}H_{37}ClFN_5O_7$ 752.22632, found 752.22893. UPLC retention time: 5.742 min.

4.3.3. 2-(1-(4-chlorobenzoyl)-5-methoxy-2-methyl-1H-indol-3-yl)-N-(10-((2-(2,6-dioxopiperidin-3-yl)-6-fluoro-1,3-dioxoisoindolin-5-yl)amino) decyl)acetamide (14)

General Procedure A (4 h) was followed by using **1** (0.026 g, 0.072 mmol) and **42** (0.035 g, 0.072 mmol) to afford the titled compound as yellow solid (0.024 g, 43 % yield) after purification by automated flash column chromatography on SiO_2 cartridge (DCM:MeOH, 99:1). ^{1}H NMR (400 MHz, $CDCl_3$) δ 8.08 (s, 1H), 7.66 (d, J = 7.8 Hz, 2H), 7.48 (d, J = 7.8 Hz, 2H), 7.39 (d, J = 9.9 Hz, 1H), 7.07 (d, J = 6.8 Hz, 1H), 6.94–6.81 (m, 2H), 6.69 (d, J = 8.6 Hz, 1H), 5.59 (bs, 1H), 4.97–4.85 (m, 1H), 4.68 (bs, 1H), 3.81 (s, 3H), 3.63 (s, 2H), 3.38–3.07 (m, 4H), 2.97–2.67 (m, 3H), 2.38 (s, 3H), 2.19–2.07 (m, 1H), 1.73–1.56 (m, 2H), 1.53–1.05 (m, 14H). ^{13}C NMR (101 MHz, $CDCl_3$) δ 170.86 (2C), 168.38, 168.19, 167.44, 166.88 (d, J = 3.0 Hz), 153.64 (d, J = 247.8 Hz), 152.41, 142.69 (d, J = 12.7 Hz), 139.64, 136.31, 133.57, 131.23 (2C), 130.90, 130.31, 130.16 (d, J = 2.3 Hz), 129.25 (2C), 118.19 (d, J = 8.9 Hz), 115.12, 112.95, 112.41, 110.02 (d, J = 22.4 Hz), 105.49 (d, J = 5.3 Hz), 100.78, 55.76, 49.27, 43.24, 39.64, 32.34, 31.45, 29.55, 29.33, 29.31, 29.16, 29.13, 28.93, 26.82, 26.74, 22.76, 13.28. HRMS m/z [M+Na]+ calcd for $C_{42}H_{45}ClFN_5O_7$ 808.28892, found 808.28914. UPLC retention time: 6.841 min.

4.3.4. 2-(2,6-dioxopiperidin-3-yl)-5,6-difluoroisoindoline-1,3-dione (36)

The mixture of 4,5-difluorophtalic anhydride (1.000 g, 5.431 mmol), potassium acetate (1.642 g, 16.836 mmol), and 3-aminopiperidin-2,6-dione hydrochloride (0.889 g, 5.975 mmol) in acetic acid (7.0 mL) was heated at 110 °C for 4h. After cooling, the reaction mixture was poured in ice-water yielding a light-purple solid which was collected by filtration, dried, and then purified by automated flash chromatography on SiO_2 cartridge (PE/EA, 6:4) to afford the titled compound as white solid (1.182 g, 75 % yield). ^{1}H NMR (400 MHz, DMSO-d_6) δ 11.15 (s, 1H), 8.16 (t, J = 7.7 Hz, 2H), 5.17 (dd, J = 12.9, 5.4 Hz, 1H), 2.96–2.81 (m, 1H), 2.69–2.44 (m, 2H), 2.12–2.01 (m, 1H).

4.3.5. tert-butyl (4-((2-(2,6-dioxopiperidin-3-yl)-6-fluoro-1,3-dioxoisoindolin-5-yl)amino)butyl)carbamate (37)

Under nitrogen atmosphere, to a stirring solution of 2-(2,6-dioxopiperidin-3-yl)-5,6-difluoroisoindoline-1,3-dione **36** (0.100 g, 0.339 mmol) in dry DMSO (3.0 mL) *tert*-butyl (4-aminobutyl)carbamate (0.065 mL, 0.339 mmol) and DIPEA (0.15 mL, 0.849 mmol) were added and the mixture was stirred at 110 °C for 3 h. The mixture was poured in ice-water yielding a precipitate which was collected by filtration. The solid was purified by automated flash chromatography on SiO_2 cartridge (DCM/MeOH, 99:1 to 98:2) to afford the titled compound as yellow solid (0.084 g, 54 % yield). ^{1}H NMR (400 MHz, $CDCl_3$) δ 8.23 (bs, 1H), 7.37 (d, J = 9.8 Hz, 1H), 7.04 (d, J = 7.0 Hz, 1H), 4.97–4.87 (m, 1H), 4.80 (bs, 1H), 4.62 (t, J = 5.0 Hz, 1H), 3.28 (t, J = 6.7 Hz, 2H), 3.23–3.10 (m, 2H), 2.94–2.67 (m, 3H), 2.16–2.08 (m, 1H), 1.77–1.57 (m, 4H), 1.44 (s, 9H).

4.3.6. tert-butyl (6-((2-(2,6-dioxopiperidin-3-yl)-6-fluoro-1,3-dioxoisoindolin-5-yl)amino)hexyl)carbamate (38)

Under nitrogen atmosphere, to a stirring solution of **36** (0.100 g, 0.339 mmol), *tert*-butyl (6-aminohexyl)carbamate (0.076 mL, 0.339 mmol) in dry DMSO (3.0 mL) and DIPEA (0.15 mL, 0.849 mmol) were added, and the mixture was stirred at 110 °C for 3 h. The mixture was poured in ice-water yielding a precipitate collected by filtration. The solid was purified by automated flash chromatography on SiO_2 cartridge (DCM/MeOH, 99:1 to 97:3) to afford the titled compound as yellow solid (0.067 g, 40 % yield). ^{1}H NMR (400 MHz, $CDCl_3$) δ 8.00 (s, 1H), 7.40 (d, J = 9.9 Hz, 1H), 7.07 (d, J = 7.1 Hz, 1H), 4.96–4.87 (m, 1H), 4.71 (bs, 1H), 4.53 (bs, 1H), 3.26 (t, J = 7.1 Hz, 2H), 3.19–3.07 (m, 2H), 2.94–2.66 (m, 3H), 2.16–2.06 (m, 1H), 1.75–1.32 (m, 17H).

4.3.7. tert-butyl (10-((2-(2,6-dioxopiperidin-3-yl)-6-fluoro-1,3-dioxoisoindolin-5-yl)amino)decyl)carbamate (39)

Under nitrogen atmosphere, to a stirring solution of **36** (0.100 g, 0.339 mmol) in dry DMSO (3.0 mL) *tert*-butyl (10-aminodecyl)carbamate [89] (0.110 g, 0.339 mmol) and DIPEA (0.15 mL, 0.849 mmol) were added, and the mixture was stirred at 110 °C for 3 h. The mixture was poured in ice-water yielding a precipitate collected by filtration. The solid was purified by automated flash chromatography on SiO_2 cartridge (DCM/MeOH, 99:1 to 97:3) to afford the titled compound as yellow solid (0.074 g, 40 % yield). ^{1}H NMR (400 MHz, $CDCl_3$) δ 8.30 (s, 1H), 7.38 (d, J = 9.9 Hz, 1H), 7.06 (d, J = 7.0 Hz, 1H), 4.99–4.85 (m, 1H), 4.53 (bs, 1H), 3.25 (t, J = 7.2 Hz, 2H), 3.17–3.03 (m, 2H), 2.92–2.67 (m, 3H), 2.15–2.05 (m, 1H), 1.74–1.61 (m, 2H), 1.51–1.18 (m, 23H).

4.3.8. 5-((4-aminobutyl)amino)-2-(2,6-dioxopiperidin-3-yl)-6-fluoroisoindoline-1,3-dione hydrochloride (40)

General Procedure B (3 h) was followed by using **37** (0.075 g, 0.162 mmol) and 4.0 N HCl in dioxane (0.75 mL) to afford the titled compound as a white solid (0.064 g, 98 % yield). ^{1}H NMR (400 MHz, DMSO-d_6) δ 11.08 (bs, 1H), 8.03–7.80 (m, 3H), 7.63–7.53 (m, 1H), 7.21–7.11 (m, 1H), 6.97 (bs, 1H), 5.11–5.02 (m, 1H), 3.59–3.57 (m, 1H), 2.95–2.74 (m, 3H), 2.64–2.54 (m, 1H), 2.06–1.97 (m, 1H), 1.68–1.58 (m, 4H).

4.3.9. 5-((6-aminohexyl)amino)-2-(2,6-dioxopiperidin-3-yl)-6-fluoroisoindoline-1,3-dione hydrochloride (41)

General Procedure B (3 h) was followed by using **38** (0.060 g, 0.122 mmol) and 4.0 N HCl in dioxane (0.6 mL) to afford the titled compound as a white solid (0.048 g, 92 % yield). ^{1}H NMR (400 MHz, DMSO-d_6) δ 11.08 (s, 1H), 7.92 (bs, 3H), 7.56 (d, J = 10.2 Hz, 1H), 7.10 (d, J = 7.2 Hz, 1H), 6.94 (bs, 1H), 5.13–4.96 (m, 1H), 3.31–3.20 (m, 2H), 2.95–2.81 (m, 1H), 2.81–2.68 (m, 2H), 2.65–2.51 (m, 2H), 2.08–1.94 (m, 1H), 1.67–1.49 (m, 4H), 1.43–1.29 (m, 4H).

4.3.10. 5-((10-aminodecyl)amino)-2-(2,6-dioxopiperidin-3-yl)-6-fluoroisoindoline-1,3-dione hydrochloride (42)

General Procedure B (3 h) was followed by using **39** (0.067 g, 0.122 mmol) and 4.0 N HCl in dioxane (0.6 mL) to afford the titled compound as a white solid (0.050 g, 86 % yield). ^{1}H NMR (400 MHz, MeOD) δ 7.43 (d, J = 10.3 Hz, 1H), 7.12 (d, J = 7.2 Hz, 1H), 5.13–5.02 (m, 1H), 3.34–3.32 (m, 2H), 2.94–2.65 (m, 5H), 2.16–2.07 (m, 1H), 1.73–1.59 (m, 4H), 1.52–1.33 (m, 12H).

4.4. Synthesis of negative control compound 15

(2*S*,4*S*)-1-((*S*)-2-(4-(4-(2-(2-(1-(4-chlorobenzoyl)-5-methoxy-2-methyl-1*H*-indol-3-yl)acetamido)ethyl)piperazin-1-yl)-4-oxobutanamido)-3,3-dimethylbutanoyl)-4-hydroxy-*N*-((*S*)-1-(4-(4-methylthiazol-5-yl)phenyl)ethyl)pyrrolidine-2-carboxamide (15). General Procedure A (3 h) was followed by using **43** (0.070 g, 0.123 mmol) and **44** (0.059 g, 0.123 mmol) to afford the titled compound as a clear yellow solid (0.026 g, 21 % yield) after purification by automated flash column chromatography on SiO_2 cartridge (DCM/MeOH, 97:3). ^{1}H NMR (400 MHz, $CDCl_3$) δ 8.67 (s, 1H), 7.69–7.57 (m, 3H), 7.48 (d, J = 8.2 Hz, 2H), 7.44–7.33 (m, 4H), 6.91–6.83 (m, 2H), 6.69 (dd, J = 8.8, 2.2 Hz, 2H), 6.16 (bs, 1H), 5.44 (d, J = 9.6 Hz, 1H), 5.13–5.03 (m, 1H), 4.73 (d, J = 9.0 Hz, 1H), 4.54–4.39 (m, 2H), 3.91 (d, J = 3.8 Hz, 1H), 3.85–3.75 (m, 4H), 3.64 (s, 2H), 3.39–3.04 (m, 6H), 2.63–2.09 (m, 18H), 1.49 (d, J = 6.9 Hz, 3H), 1.05 (s, 9H). ^{13}C NMR (101 MHz, $CDCl_3$) δ 172.41, 172.35, 171.56 (2C), 169.95, 169.75, 168.33, 156.23, 150.32, 148.62, 142.36, 139.76, 136.25, 133.42, 131.42, 131.22 (2C), 130.94, 130.33, 129.66 (2C), 129.29 (2C), 126.48 (2C), 114.96, 112.99, 111.92, 101.22, 71.07, 59.91, 58.66, 57.32, 56.14, 55.79, 52.53, 52.26, 49.26, 45.00, 41.60, 35.86, 35.17, 34.75, 32.17, 31.10, 28.48, 26.46 (3C), 21.90, 16.12, 13.25. HRMS (ESI) m/z $[M + Na]^+$ calcd for $C_{52}H_{63}ClN_8O_8S$ 1017.40703, found 1017.41154. UPLC retention time: 5.004 min.

4.4.1. 4-(4-(2-(2-(1-(4-chlorobenzoyl)-5-methoxy-2-methyl-1H-indol-3-yl)acetamido)ethyl)piperazin-1-yl)-4-oxobutanoic acid (43)

Under nitrogen atmosphere, to a stirred solution of **33** [66] (0.187 g, 0.399 mmol) in dry DCM (2.0 mL), dihydrofuran-2,5-dione (0.040 g, 0.399 mmol) and Et_3N (0.056 mL, 0.399 mmol) were added. The reaction was stirred at room temperature for 5 h. Then, the mixture was evaporated *in vacuo*, tritured with Et_2O and collected by filtration to give the titled compound as a clear yellow solid (0.223 g, 98 % yield). ^{1}H NMR (400 MHz, $CDCl_3$) δ 11.90 (bs, 1H), 10.19 (bs, 1H), 7.77–7.57 (m, 4H), 7.16 (s, 1H), 6.94 (d, $J = 9.0$ Hz, 1H), 6.72 (d, $J = 8.9$ Hz, 1H), 3.77 (s, 3H), 3.67–3.17 (m, 10H), 2.75–2.54 (m, 4H), 2.46–2.40 (m, 4H), 2.25 (s, 3H).

4.5. Synthesis of negative control compound 16

4.5.1. (2S,4S)-1-((S)-2-(2-(4-(2-(1-(4-chlorobenzoyl)-5-methoxy-2-methyl-1H-indol-3-yl)acetyl)piperazin-1-yl)acetamido)-3,3-dimethylbutanoyl)-4-hydroxy-N-((S)-1-(4-(4-methylthiazol-5-yl)phenyl)ethyl)pyrrolidine-2-carboxamide (16)

General Procedure A (2 h) was followed by using **1** (0.059 g, 0.165 mmol) and **46** (0.100 g, 0.165 mmol) to afford the titled compound as a clear yellow solid (0.033 g, 22 % yield) after purification by automated flash column chromatography on SiO_2 cartridge (DCM/MeOH, 95:5). ^{1}H NMR (400 MHz, $CDCl_3$) δ 8.68 (s, 1H), 7.70–7.60 (m, 3H), 7.53–7.40 (m, 5H), 7.40–7.33 (m, 2H), 6.96 (d, $J = 2.3$ Hz, 1H), 6.79 (d, $J = 9.0$ Hz, 1H), 6.65 (dd, $J = 9.0$, 2.4 Hz, 1H), 5.40 (d, $J = 9.6$ Hz, 1H), 5.14–5.04 (m, 1H), 4.73 (d, $J = 9.0$ Hz, 1H), 4.53–4.43 (m, 2H), 3.96 (dd, $J = 10.9$, 4.0 Hz, 1H), 3.86–3.55 (m, 10H), 3.02 (s, 2H), 2.62–2.32 (m, 11H), 2.16–2.08 (m, 1H), 1.50 (d, $J = 6.9$ Hz, 3H), 1.07 (s, 9H). ^{13}C NMR (101 MHz, $CDCl_3$) δ 172.05, 171.41, 169.51, 168.73, 168.25, 156.01, 150.35, 148.64, 142.26, 139.38, 135.28, 133.80, 131.38, 131.29, 131.21 (2C), 130.85, 130.60, 129.68 (2C), 129.15 (2C), 126.47 (2C), 114.89, 113.01, 111.42, 101.65, 77.33, 77.01, 76.69, 71.02, 61.23, 59.88, 58.81, 56.75, 55.76, 53.43, 53.22, 49.26, 45.89, 42.08, 35.04, 34.64, 30.26, 26.50 (3C), 21.88, 16.11, 13.44. HRMS (ESI) *m/z* $[M + Na]^+$ calcd for $C_{48}H_{56}ClN_7O_7S$ 910.37232, found 910.37672. UPLC retention time: 5.469 min.

4.5.2. Tert-butyl 4-(2-(((S)-1-((2S,4S)-4-hydroxy-2-(((S)-1-(4-(4-methylthiazol-5-yl)phenyl)ethyl)carbamoyl)pyrrolidin-1-yl)-3,3-dimethyl-1-oxobutan-2-yl)amino)-2-oxoethyl)piperazine-1-carboxylate (45)

General Procedure A (3 h) was followed by using **44** (0.150 g, 0.312 mmol) and 2-(4-(*tert*-butoxycarbonyl)piperazin-1-yl)acetic acid (0.076 g, 0.312 mmol) to afford the titled compound as a white solid (0.141 g, 67 % yield) after purification by flash column chromatography on SiO_2 (DCM/MeOH, 95:5). ^{1}H NMR (400 MHz, $CDCl_3$) δ 8.68 (s, 1H), 7.74 (d, $J = 8.7$ Hz, 1H), 7.55 (d, $J = 7.7$ Hz, 1H), 7.40 (dd, $J = 23.7$, 8.3 Hz, 4H), 5.40 (d, $J = 9.6$ Hz, 1H), 5.14–5.03 (m, 1H), 4.75 (d, $J = 8.7$ Hz, 1H), 4.56–4.40 (m, 2H), 3.98 (dd, $J = 10.8$, 4.1 Hz, 1H), 3.81 (d, $J = 11.1$ Hz, 1H), 3.48 (s, 4H), 3.04 (s, 2H), 2.56–2.46 (m, 7H), 2.36 (d, $J = 14.2$ Hz, 1H), 2.21–2.08 (m, 1H), 1.50 (d, $J = 6.9$ Hz, 3H), 1.46 (s, 9H), 1.07 (s, 9H).

(2*S*,4*S*)-1-((*S*)-3,3-dimethyl-2-(2-(piperazin-1-yl)acetamido) butanoyl)-4-hydroxy-*N*-((*S*)-1-(4-(4-methylthiazol-5-yl)phenyl) ethyl)pyrrolidine-2-carboxamide hydrochloride (46). General Procedure B (2 h) was followed by using **45** (0.140 g, 0.209 mmol) and 4.0 N HCl in dioxane (1.4 mL) to afford the titled compound as a white solid (0.123 g, 97 % yield). ^{1}H NMR (400 MHz, DMSO-d_6) δ 10.01 (bs, 2H), 9.07 (s, 1H), 8.69 (d, $J = 7.9$ Hz, 1H), 8.43 (d, $J = 7.4$ Hz, 1H), 7.48–7.39 (m, 4H), 4.97–4.90 (m, 1H), 4.48 (d, $J = 8.4$ Hz, 1H), 4.40–4.33 (m, 1H), 4.25–4.06 (m, 3H), 3.93–3.85 (m, 1H), 3.56–3.35 (m, 8H), 2.47 (s, 3H), 2.40–2.29 (m, 1H), 1.71–1.61 (m, 1H), 1.39 (d, $J = 6.8$ Hz, 3H), 1.35–1.25 (m, 1H), 0.99 (s, 9H).

4.6. Synthesis of VHL ligand 17

4.6.1. (S)-tert-butyl (1-(4-bromophenyl)ethyl)carbamate (47)

To the solution of (*S*)-1-(4-bromophenyl)ethanamine (0.500 g, 2.499 mmol) in EA (2.5 mL), a solution of $NaHCO_3$ (0.150 g, 1.785 mmol) in water (2.5 mL) was added. To this mixture, a solution of Boc_2O (0.662 g, 3.034 mmol) in EA (1.0 mL) was added dropwise at room temperature. The reaction was stirred at room temperature for 18 h. Then, the mixture was extracted with EA (50 mL x 3), the reunited organic phases were washed with water (50 mL), brine (50 mL), dried over Na_2SO_4 and evaporated to dryness to give a colourless oil which solidified upon standing (0.749 g, 100 % yield). ^{1}H NMR (400 MHz, $CDCl_3$) δ 7.48–7.42 (m, 2H), 7.17 (d, $J = 8.4$ Hz, 2H), 4.75 (bs, 2H), 1.50–1.33 (m, 12H).

4.6.2. (S)-tert-butyl (1-(4-(4-methylthiazol-5-yl)phenyl)ethyl)carbamate (48)

47 (0.749 g, 2.495 mmol), 4-methylthiazole (0.570 g, 5.738 mmol), and AcOK (0.563 g, 5.738 mmol) in dry DMA (5.4 mL) were degassed under nitrogen for 10 min and then $Pd(OAc)_2$ (0.034 g, 0.149 mmol) was added. The reaction mixture was stirred at 130 °C for 4 h. After cooling to room temperature, the reaction mixture was filtered through a short pad of Celite. The filtrate was diluted with EA (60.0 mL), washed with water (30 mL x 2), brine (30 mL), dried over anhydrous Na_2SO_4 and concentrated under reduced pressure to afford the desired compound as a grey residue (0.655 g) which was used directly for the next step.

4.6.3. (S)-1-(4-(4-methylthiazol-5-yl)phenyl)ethanamine hydrochloride (49)

To the solution of **48** (0.655 g, 2.057 mmol) in dry DCM (1.5 mL), 4.0 N HCl in dioxane (3.7 mL) was added dropwise at 0 °C. The reaction was stirred at room temperature for 18 h. Then, the solvent was evaporated to dryness and the residue was tritured with DEE (10 mL), collected by filtration, and dried *in vacuo* to afford the titled compound as a light brown solid (0.523 g, two-step yield 99.8 %). ^{1}H NMR (400 MHz, DMSO-d_6) δ 9.09 (s, 1H), 8.67 (bs, 3H), 7.69–7.52 (m, 4H), 4.52–4.36 (m, 1H), 2.47 (s, 3H), 1.55 (d, $J = 6.8$ Hz, 3H).

4.6.4. (2S,4R)-tert-butyl 4-hydroxy-2-(((S)-1-(4-(4-methylthiazol-5-yl) phenyl)ethyl)carbamoyl)pyrrolidine-1-carboxylate (50)

Under nitrogen atmosphere, to a stirred solution of **49** (0.650 g, 2.551 mmol) in dry DMF (3 mL) and dry DCM (3 mL), Et_3N (1.08 mL, 7.77 mmol), (2*S*,4*S*)-1-(*tert*-butoxycarbonyl)-4-hydroxypyrrolidine-2-carboxylic acid (0.601 g, 2.602 mmol) and HATU (1.181 g, 3.106 mmol) were added at 0 °C. The mixture was stirred for 1 h at 0 °C and then for 17 h at room temperature. Then, DCM was evaporated *in vacuo* and to the residue was added saturated $NaHCO_3$ solution (60 mL). The reaction was extracted with EA (40 mL x 3), washed with water (20 mL x 2), brine (20 mL), dried over anhydrous Na_2SO_4 and concentrated under reduced pressure to afford the desired compound as a yellow solid (1.038 g) which was used directly for the next step.

4.6.5. (2S,4R)-4-hydroxy-N-((S)-1-(4-(4-methylthiazol-5-yl)phenyl) ethyl)pyrrolidine-2-carboxamide hydrochloride (52)

To the solution of **50** (1.0 g, 2.317 mmol) in dioxane (3.2 mL) and EA (0.8 mL), 4.0 N HCl in dioxane (4.4 mL) was added dropwise at 0 °C. The reaction was stirred at room temperature for 18 h. Then, the solvent was evaporated to dryness and the residue was tritured with DEE (10 mL), collected by filtration, and dried *in vacuo* to afford the titled compound as a yellow solid (0.852 g, two-step yield 100 %). ^{1}H NMR (400 MHz, DMSO-d_6) δ 10.16 (bs, 1H), 9.28 (d, $J = 7.5$ Hz, 1H), 9.09 (s, 1H), 8.58 (bs, 1H), 7.44 (dd, $J = 25.3$, 8.2 Hz, 4H), 5.06–4.93 (m, 1H), 4.45–4.36 (m, 2H), 3.35–3.24 (m, 1H), 3.12–3.03 (m, 1H), 2.68 (s, 3H), 2.46 (s, 3H), 2.40–2.31 (m, 1H), 1.84–1.75 (m, 1H), 1.42 (d, $J = 6.9$ Hz, 3H).

4.6.6. Tert-butyl ((S)-1-((2S,4R)-4-hydroxy-2-(((S)-1-(4-(4-methylthiazol-5-yl)phenyl)ethyl)carbamoyl)pyrrolidin-1-yl)-3,3-dimethyl-1-oxobutan-2-yl)carbamate (54)

Under nitrogen atmosphere, to a stirred solution of (*S*)-2-((*tert*-butoxycarbonyl)amino)-3,3-dimethylbutanoic acid (0.953 g, 4.123 mmol) in dry DCM (10.5 mL), DIPEA (1.8 mL, 10.307 mmol) and HATU (1.834 g, 4.824 mmol) were added at 0 °C. After 1 h, **52** (0.910 g, 2.473 mmol) was added slowly. The mixture was stirred for 18 h at room temperature. Then, DCM (50 mL) was added to the reaction mixture and was washed with 10 % citric acid (12 mL) twice, saturated $NaHCO_3$ solution (12 mL) twice, water (12 mL) twice, and brine (20 mL) once. The organic phase was dried over anhydrous Na_2SO_4 and concentrated under reduced pressure to afford the desired compound as a yellow oil (1.873 g) which was used directly for the next step.

4.6.7. (2S,4R)-1-((S)-2-amino-3,3-dimethylbutanoyl)-4-hydroxy-N-((S)-1-(4-(4-methylthiazol-5-yl)phenyl)ethyl)pyrrolidine-2-carboxamide hydrochloride (17)

To a solution of **54** in a mixture of dry DCM (6.0 mL) and dry MeOH (2.0 mL), 4.0 N HCl in dioxane (4.7 mL) was added dropwise at 0 °C for over 30 min. The mixture was stirred at room temperature overnight. Then, the reaction mixture was concentrated, water (50 mL) was added, and the solution was extracted with DCM (20 mL x 3). The aqueous phase was then transferred to a beaker, and solid $NaHCO_3$ (2.5 g) was added to the solution to adjust the pH to 8. Then, the aqueous phase was extracted with DCM (30 mL x 3); the reunited organic phase was washed with brine (20 mL), dried over Na_2SO_4 and concentrated *in vacuo*. The resulting beige foam was dissolved in dioxane (20 mL), and 4.0 N HCl in dioxane (3.0 mL) was added dropwise for over 30 min at 0 °C. The resulting mixture was concentrated *in vacuo* and dissolved in MeOH (7.0 mL). The solution was added dropwise to EA (60.0 mL) over 2 h. The precipitated solid was filtered and dried *in vacuo* to give a 0.664 g beige solid (two-step yield 68 %; and overall yield 60 %). ^{1}H NMR (400 MHz, DMSO-d_6) 9.08 (s, 1H), 8.61 (d, $J = 7.6$ Hz, 1H), 8.16 (bs, 3H), 7.42 (dd, $J = 25.4$, 8.1 Hz, 4H), 4.99–4.85 (m, 1H), 4.58–4.51 (m, 1H), 4.34–4.27 (m, 1H), 3.92–3.84 (m, 1H), 3.79–3.70 (m, 1H), 3.55–3.44 (m, 1H), 2.46 (s, 3H), 2.16–2.06 (m, 1H), 1.81–1.69 (m, 1H), 1.38 (d, $J = 6.9$ Hz, 3H), 1.02 (s, 9H). ^{13}C NMR (101 MHz, DMSO-d_6) δ 170.68, 167.08, 152.32, 147.62, 145.27, 131.88, 129.91, 129.32 (2C), 126.84 (2C), 69.35, 60.22, 59.30, 58.51, 56.94, 48.24, 34.85, 26.54 (3C), 22.97, 16.20. HRMS (ESI) *m/z* $[M + H]^+$ calcd for $C_{23}H_{32}N_4O_3S$ 445.22679, found 445.2275. UPLC retention time: 3.211 min.

4.7. Synthesis of VHL ligand 44

4.7.1. (2S,4S)-tert-butyl 4-hydroxy-2-(((S)-1-(4-(4-methylthiazol-5-yl)phenyl)ethyl)carbamoyl)pyrrolidine-1-carboxylate (51)

Under nitrogen atmosphere, to a stirred solution of **49** (0.523 g, 2.052 mmol) in dry DMF (3 mL) and dry DCM (3 mL), Et_3N (1.08 mL, 7.77 mmol), (2*S*,4*S*)-1-(*tert*-butoxycarbonyl)-4-hydroxypyrrolidine-2-carboxylic acid (0.484 g, 2.093 mmol) and HATU (1.181 g, 3.106 mmol) were added at 0 °C. The mixture was stirred for 1 h at 0 °C and then for 17 h at room temperature. Then, DCM was evaporated *in vacuo* and to the residue was added saturated $NaHCO_3$ solution (60 mL). The reaction was extracted with EA (40 mL x 3), washed with water (20 mL x 2), brine (20 mL), dried over anhydrous Na_2SO_4 and concentrated under reduced pressure to afford the desired compound as a yellow solid (0.888 g) which was used directly for the next step.

4.7.2. (2S,4S)-4-hydroxy-N-((S)-1-(4-(4-methylthiazol-5-yl)phenyl)ethyl)pyrrolidine-2-carboxamide hydrochloride (53)

To the solution of **51** (0.888 g, 2.057 mmol) in dioxane (2.8 mL) and EA (0.7 mL), 4.0 N HCl in dioxane (3.9 mL) was added dropwise at 0 °C. The reaction was stirred at room temperature for 18 h. Then, the solvent was evaporated to dryness and the residue was tritured with DEE (10 mL), collected by filtration, and dried *in vacuo* to afford the titled compound as a yellow solid (0.754 g, two-step yield 99.6 %). ^{1}H NMR (400 MHz, DMSO-d_6) δ 10.16 (bs, 1H), 9.28 (d, $J = 7.5$ Hz, 1H), 9.09 (s, 1H), 8.58 (bs, 1H), 7.50–7.38 (m, 8.2 Hz, 4H), 5.06–4.93 (m, 1H), 4.45–4.33 (m, 2H), 3.35–3.24 (m, 1H), 3.12–3.03 (m, 1H), 2.68 (s, 3H), 2.46 (s, 3H), 2.40–2.31 (m, 1H), 1.84–1.75 (m, 1H), 1.42 (d, $J = 6.9$ Hz, 3H).

4.7.3. Tert-butyl ((S)-1-((2S,4S)-4-hydroxy-2-(((S)-1-(4-(4-methylthiazol-5-yl)phenyl)ethyl)carbamoyl)pyrrolidin-1-yl)-3,3-dimethyl-1-oxobutan-2-yl)carbamate (55)

Under nitrogen atmosphere, to a stirred solution of (*S*)-2-((*tert*-butoxycarbonyl)amino)-3,3-dimethylbutanoic acid (0.790 g, 3.416 mmol) in dry DCM (8.7 mL), DIPEA (1.5 mL, 8.540 mmol) and HATU (1.520 g, 3.997 mmol) were added at 0 °C. After 1 h, **53** (0.754 g, 2.049 mmol) was added slowly. The mixture was stirred for 18 h at room temperature. Then, DCM (50 mL) was added to the reaction mixture and was washed with 10 % citric acid (12 mL) twice, saturated $NaHCO_3$ solution (12 mL) twice, water (12 mL) twice, and brine (20 mL) once. The organic phase was dried over anhydrous Na_2SO_4 and concentrated under reduced pressure to afford the desired compound as a yellow oil (1.114 g) which was used directly for the next step.

4.7.4. (2S,4S)-1-((S)-2-amino-3,3-dimethylbutanoyl)-4-hydroxy-N-((S)-1-(4-(4-methylthiazol-5-yl)phenyl)ethyl)pyrrolidine-2-carboxamide hydrochloride (44)

To a solution of **55** in a mixture of dry DCM (3.5 mL) and dry MeOH (1.2 mL), 4.0 N HCl in dioxane (2.8 mL) was added dropwise at 0 °C for over 30 min. The mixture was stirred at room temperature overnight. Then, the reaction mixture was concentrated, water (50 mL) was added, and the solution was extracted with DCM (20 mL x 3). The aqueous phase was then transferred to a beaker, and solid $NaHCO_3$ (2.0 g) was added to the solution to adjust the pH to 8. Then, the aqueous phase was extracted with DCM (30 mL x 3); the reunited organic phase was washed with brine (20 mL), dried over Na_2SO_4 and concentrated *in vacuo*. The resulting beige foam was dissolved in dioxane (20 mL), and 4.0 N HCl in dioxane (2.0 mL) was added dropwise for over 30 min at 0 °C. The resulting mixture was concentrated *in vacuo* and dissolved in MeOH (7.0 mL). The solution was added dropwise to EA (60.0 mL) over 2 h. The precipitated solid was filtered and dried *in vacuo* to give a 0.664 g beige solid (two-step yield 67 % and overall yield 66 %). ^{1}H NMR (400 MHz, DMSO-d_6) δ 9.14 (s, 1H), 8.60 (d, $J = 7.5$ Hz, 1H), 8.22 (bs, 3H), 7.54–7.35 (m, 4H), 5.00–4.86 (m, 1H), 4.42 (t, $J = 7.9$ Hz, 1H), 4.23–4.14 (m, 1H), 4.05–3.95 (m, 1H), 3.94–3.83 (m, 1H), 3.28–3.17 (m, 1H), 2.47 (s, 3H), 2.43–2.34 (m, 1H), 1.67–1.54 (m, 1H), 1.38 (d, $J = 6.9$ Hz, 3H), 1.02 (s, 9H). ^{13}C NMR (101 MHz, DMSO-d_6) δ 170.80, 167.25, 152.51, 147.33, 145.11, 132.03, 129.84, 129.33 (2C), 126.89 (2C), 69.10, 58.91, 58.37, 55.61, 48.31, 37.35, 34.61, 26.54 (3C), 22.83, 16.06. HRMS (ESI) *m/z* $[M + Na]^+$ calcd for $C_{23}H_{32}N_4O_3S$ 467.20873, found 467.2092. UPLC retention time: 3.153 min.

4.8. Biological activity

4.8.1. Cells and Viruses

African Green Monkey Vero E6 cells (ATCC® CRL-1586™), MRC-5 cells (ATCC® CCL-171™), and Human Embryonic Kidney (HEK) 293T cells (ATCC® CRL-3216™) were cultured in DMEM supplemented with 10 % fetal bovine serum (FBS, Life Technologies), while HCT-8 cells (ATCC® CCL-244) were cultured in RPMI supplemented with 10 % FBS. Calu-3 cells (AddexBio, #C0016001) were cultured in EMEM supplemented with nonessential amino acids and 10 % FBS. All cells were cultured in the presence of 100 U/mL penicillin and 100 μg/mL streptomycin (Life Technologies), were maintained at 37 °C in a humidified atmosphere supplemented with 5 % CO_2, and periodically tested for the absence of mycoplasma contamination.

SARS-CoV-2/NL/2020 strain was obtained from European Virus Archive Global (EVAg) and was propagated and titrated in Vero E6 cells.

HCoV-OC43 (VR-1558™) and HCoV-229E (VR-740™) strains were purchased from ATCC and were propagated in HCT-8 and MRC-5 cells, respectively.

4.8.2. Antiviral assays

Plaque reduction assays (PRA) with different CoVs were performed as previously described [27]. For virus yield reduction assays of SARS-CoV-2 in Calu-3 cells, a protocol previously described was followed [75]. All work with infectious SARS-CoV-2 virus was performed in a biosafety level 3 (BSL3) laboratory according to the safety practices as approved by the Department of Molecular Medicine (University of Padua, Italy) Committee on Microbiological Safety.

4.8.3. Cell viability assays

The effect on cell viability of test compounds was determined in Vero E6, MRC-5, and Calu-3 cells at 72 h by the 3-(4,5-dimethylthiazol-2-yl)-2,5-diphenyl tetrazolium bromide (MTT; Sigma-Aldrich) or Alamar Blue (ThermoFisher) method as described previously [90].

4.8.4. Cell-based assays to detect PGES-2 and M^{pro} degradation

For the detection of PGES-2 degradation in uninfected cells, 293T, Vero E6, and MRC-5 cells were seeded at a density of 2×10^5, 1 x 10^5, and 6×10^4 cells/well, respectively, in 24-well plates. The next day, cells were treated with test compounds or 0.1 % DMSO as a control and collected at different times post-treatment. For the detection of PGES-2 degradation in infected cells, Vero E6 and MRC-5 cells were seeded at a density of 1×10^5 and 6×10^4 cells/well, respectively, in 24-well plates. The next day, Vero E6 and MRC-5 cells were infected with SARS-CoV-2 and HCoV-OC43 or HCoV-229E, respectively. After 90 min at 37 °C, the viral inoculum was removed and cells were treated with test compounds or 0.1 % DMSO as a control and collected at different time-points.

For the detection of M^{pro} degradation in transfected 293T cells, cells were seeded at a density of 2×10^5 cells/well in 24-well plates. The next day, cells were pre-treated for 2 h with test compounds or 0.1 % DMSO as a control and then were transfected with 100 ng of pcDNA-FLAG-nsp4-M^{pro} using Lipofectamine 2000 (ThermoFisher), according to the manufacturer's instructions. The pcDNA3.1-FLAG-nsp4-M^{pro} plasmid, expressing the FLAG tag fused at the N-terminus of the nsp4-M^{pro} of SARS-CoV-2, was obtained by PCR amplification of nsp4-M^{pro} sequence from pGEX-6p-1-M^{Pro} (kindly provided by Prof. Rolf Hilgenfeld, Institute of Biochemistry, Center for Structural and Cell Biology in Medicine, University of Lübeck, Germany) and subsequent cloning into pcDNA3.1-(+) (Invitrogen) at *BamHI/XhoI* sites. The pcDNA3.1-FLAG-nsp4-M^{pro} C145A plasmid, which expresses a catalytically inactive form of M^{pro}, was obtained by site-directed mutagenesis. The sequences of the oligonucleotides used are listed in Table S4. The correct sequences were verified by Sanger sequencing. After transfection, cells were incubated for 24 h in the presence of test compounds or DMSO and Boceprevir (BOC) as controls and at the end were collected for the analysis of M^{pro} degradation by Western Blot (WB). BOC and the VHL inhibitor VH298 were purchased from Selleckchem and Abcam, respectively.

For the detection of M^{pro} degradation in Calu-3 cells infected with SARS-CoV-2, cells were seeded at a density of 2×10^5 cells/well in 24-well plates and the next day infected with SARS-CoV-2/NL/2020 at MOI = 0.1 and treated with different concentrations of **6** (from 25 to 1 μM) for 48 h. At the end of incubation, cells were collected and further analyzed.

Whole-cell protein extracts were prepared as previously described [91] and then analyzed by WB with antibodies against PGES-2 (1:2,000, Invitrogen, # PA5-87300), SARS-CoV-2 M^{pro} (1:2,000, Cell Signaling, #51661), or against β-actin (1:10,000, Merck, #A5441) as a control for protein loading. Immunocomplexes were detected with goat anti-mouse immunoglobulin antibodies (Millipore, 12–349) or goat anti-rabbit (Millipore, 12–348) conjugated to horseradish peroxidase.

Concentration at half-maximal degradation activity (DC_{50}) and the % of degradation at the maximal concentration tested were determined by densitometric analysis of two-three independent experiments using ImageJ software and nonlinear regression analysis by GraphPad Prism 10.0.

4.8.5. SARS-CoV-2 M^{pro} activity assay in vitro

To evaluate the SARS-CoV-2 M^{pro} activity *in vitro,* we employed a fluorescence resonance energy transfer (FRET)-based cleavage assay with a peptide substrate as previously described [92] with minor modifications. A detailed description of the protocol followed for the expression and purification of M^{pro} and for the FRET-based assay was already reported in Ref. [75].

4.9. Microscale Thermophoresis (MST) binding assay

Recombinant M^{pro} (nsp5, $3CL^{pro}$) was produced as previously described [75] and fluorescently labelled to lysine residues with RED dye NT650, provided by NanoTemper Technologies (NanoTemper Technologies, GmbH, Munich, Germany) using a 1:3 protein/dye ratio. Briefly, 100 μL of 28 μM protein was mixed with 100 μL of 84 μM fluorophore dye and incubated for 30 min at RT in the dark condition, according to the instructions of the vendor. A buffer composed of 130 mM $NaHCO_3$, 50 mM NaCl, pH 8.2 was used for the labelling process. Unbounded dye was then removed by size-exclusion chromatography with the running buffer consisting of 20 mM Tris, 140 NaCl, pH 8.0 (Tris). Protein and RED dye concentrations were assessed using Absorbance Spectroscopy with a Thermo Scientific™ NanoDrop™ One spectrophotometer (Thermo Fisher Scientific Inc.,Waltham, MA, USA), using a protein extinction coefficient ε_{280nm} of 32890 $M^{-1}cm^{-1}$, dye ε_{650nm} of 195000 $M^{-1}cm^{-1}$, a correcting factor at 280 nm equal to 0.04 and the following equations:

$$[protein] = \frac{A_{280} - (A_{650} \times cf)}{\varepsilon_{protein} \times l} \quad \text{(eq.1)}$$

$$[dye] = \frac{A_{650}}{\varepsilon_{RED\ dye} \times l} \quad \text{(eq.2)}$$

The Degree of Labelling (DoL) was determined as the ratio between the RED dye and protein concentration in the sample and was 0.8. The stability of the protease after the labelling process and after the overnight incubation at 4 °C was checked using label-free thermal shift analysis (TSA) using Tycho NT.6 instrument (NanoTemper Technologies GmbH, Munich, Germany). Specifically, Thermal unfolding analysis monitors changes in the emission intensity and wavelength maximum of intrinsic fluorescence properties of buried tryptophane and tyrosine residues that become exposed in the unfolded state of the protein upon an increasing temperature from 35 °C to 95 °C. The samples containing 3 μM of protein in Tris buffer were loaded into Tycho NT.6 capillaries, and the thermal unfolding profiles were recorded for comparative analysis in three independent experiments. Inflection temperature (T_i) values are reported as mean ± standard deviation values (Fig. S1, Supplementary Information). The unfolding profile of labelled M^{pro} did not display a different trend from the curve of native protein and no stability shift was observed between the samples, suggesting that both the labelling process and the incubation time did not affect the stability of the protein. Standard MST binding experiments were performed in TRIS buffer, adding 0.01 % Tween20, 1 mM EDTA and 2 % DMSO. BOC and INM were tested against NT650-M^{pro} (protein concentration 20 nM) with sixteen serial dilutions starting from a compound concentration of 1 mM. After overnight incubation at +4. C in the dark, the samples were loaded into premium-coated capillaries (MO-K025; NanoTemper Technologies, Munich, Germany) and inserted in the chip tray of Monolith NT.115 instrument (NanoTemper Technologies, Munich, Germany) for thermophoresis analysis, setting LED power at 60 % and medium MST power. Recorded data were processed with NanoTemper *MO Affinity Analysis v2.3* in *DoT* (*Default on Time*), setting the *hot region* between *4/5 s*. Dissociation constants (K_d) were obtained as mean values with

confidence interval (±) that defines the range where the K_d falls with a 68 % of certainty, as declared by NanoTemper. Signal to Noise ratio (S/N) allows judging data quality: a value of more than 5 is desirable while a value of more than 12 corresponds to an excellent assay. For PROTACs **3**, **5**, and **6**, a single-point binding assay was carried out (Fig. S2). Compounds were tested at a 50 μM concentration against 20 nM NT650-M^{pro}, at the same experimental conditions used for the standard MST assays. As a rule of thumb, compounds were defined as binders when producing a fluorescent signal (F_{norm}) outside the signal value and three-fold standard deviations of the vehicle. All the experiments were run in triplicate.

4.10. Modelling studies

The crystallographic structure of indomethacin in complex with SARS-CoV-2 M^{pro} has never been reported and is not available in the Protein Data Bank [93]. Therefore, the interaction of indomethacin with SARS-CoV-2 M^{pro} (PDB ID: 6LU7) was predicted by using FLAPSite algorithm implemented in FLAP software [94,95] (developed and licensed by Molecular Discovery Ltd., UK) after having removed the carboxylic function in indomethacin ligand and leaving a methyl group in C-3 position of the scaffold. Indeed, in the tested PROTACs the carboxylic moiety is not present as that group is exploited to anchor linker moieties through amide linkage. The x-ray structure of VHL E3 ligase in complex with its ligand was extracted from the PDB ID: 5T35 [96]. As previously described [27], to predict the formation of the SARS-CoV-2 M^{pro}/PROTAC/VHL ternary complex, GRID Molecular Interaction Fields (MIFs) [97–99] were calculated at the M^{pro} catalytic site and VHL-E3 ligase protein surfaces in the proximity of the binding site, and the best complementarity of the hydrophobic and polar MIFs was used as the driving force of the ternary complex formation. Once the best orientation was found, the PROTAC was docked by overlapping the ligands onto the docking or x-ray poses and adjusting the linker to get rid of clashes and to optimize interactions. To generate the hydrophobic MIF the CRY probe was used [100], while polar interactions were evaluated using the N1 and the O probes, all within the GRID 2021 package [99].

4.11. Kinetic solubility

Kinetic solubility in universal buffer (ethanolamine 45 mM, sodium dihydrogen phosphate 45 mM, and sodium acetate 45 mM) at pH 7.4 was measured following the Millipore protocol for 96-well filtration assay [101], with minor modifications. Briefly, the aqueous buffer solution was kept at 25 °C for 30 min, and pH was adjusted to 7.4 with a 1 M solution of HCl or NaOH. Thus, 237.5 μL of universal buffer solution were added to each well of a filter plate. Afterwards, 10 μL of DMSO were transferred into each well, and aliquots of 2.5 μL of analyte DMSO solution 10 mM were added. The final concentration of the compound was 100 μM (and not 500 μM as reported in the Millipore protocol, due to the limited PROTAC solubility), while the percentage of DMSO in the aqueous buffer solution was 5 %. The filter plate was then covered and shaken on a CAPPRondo microplate shaker for 90 min (600 rpm; 25 °C). After the incubation, the solution was vacuum-filtered into a polypropylene 96-well plate with a MultiScreen®HTS Vacuum Manifold. For each well, aliquots of 160 μL of filtered solution were transferred from the 96-well plate to a 96-well disposable UV analysis plate for UV spectroscopy. Thus, 40 μL of ACN/DMSO 95/5 (% v/v) solution was dispensed in each well, and the plate was covered and gently shaken at 25 °C for 5 min.

For each compound, a full scan acquisition was performed at 5 nm increments from 230 nm to 600 nm, to determine the maximum absorption wavelength to be used for solubility determination. The solubility, expressed as the concentration of the filtered solution, was quantified using an external calibration curve. The various solutions of the calibration line (3.13 μM, 12.5 μM, 25 μM, 50 μM, 100 μM) were prepared in buffer/ACN 80/20 (% v/v), to ensure overall compound solubility. Additionally, the level of DMSO in all calibrators is maintained at 5 % (v/v), ensuring that the final solvent content of all standards and samples remains consistent. The final compound concentration in the filtered solution was determined by subtracting the intercept of the calibration curve to the absorbance and then dividing by the slope. To account for the dilution with acetonitrile prior to obtaining the absorbance spectrum values were multiplied by a factor of 1.25.

4.12. Chemical stability

For chemical stability, tested compounds (1 and 10 μM with 0.1 % DMSO) were incubated at 37 °C in DMEM cellular medium containing 10 % FBS and 100 U/mL penicillin and 100 μg/mL streptomycin (pH 7.4). Aliquots (60 μL) of the incubation mix were taken at 0 and 24 h, and added to 60 μL of ice-cold acetonitrile containing labetalol (1 μL) as internal standard. Samples were then centrifuged at 20,800*g* for 15 min at 4 °C. The supernatant first was filtered by Millex-LG filters (Merck KGaA, Darmstadt, Germany) and then concentrated by evaporation under a nitrogen stream. Residuals were suspended in DMSO and centrifuged at 20,800*g*, 25 °C for 15 min. Supernatants were retrieved for LC-MS/MS analyses. The blank was prepared similarly but in the absence of the investigated compounds. Acquisitions of the samples for chemical stability were accomplished with a Hybrid Quadrupole-Orbitrap Mass Spectrometer (Q Exactive, Thermo Fisher Scientific Inc., Waltham, MA). The instrument was equipped with a Dionex UltiMate 3000 UHPLC system including a binary pump and thermostated autosampler and column compartments. A volume of 2 μL was injected for each sample. Chromatographic separation of analytes was conducted in reverse-phase chromatography. In brief, a Luna Omega 1.6 μm Polar (C18, 2.1 mm × 150 mm) was used, and the mobile phases consisted of water (A) and acetonitrile (B), both containing formic acid at 0.1 %. The LC flow was set at 0.400 mL/min in a 12 min gradient elution as follows: 99.5:0.5 (A/B) to 5:95 (A/B) over 10 min, 5:95 (A/B) for 2 min, and then reversion back to 99.5:0.5 (A/B) over 2.5 min. The column was operating at a constant temperature of 40 °C. The LC effluents were introduced into the Q-Exactive mass spectrometer by an H-ESI source that operated in the positive mode with a sheath gas flow rate of 45; an auxiliary gas flow rate of 15; a spray voltage of 3.5 kV; capillary temperature and auxiliary gas heater temperature, respectively, of 320 and 350 °C; and S-lens RF level 50. The Q-Exactive mass spectrometer operates in the data-dependent scan (DDS) mode, with a resolution of 70.000 in full mass and 17.500 in MS/MS, in the scan mass range of 100–1500 at collision energies of 15, 60, and 120 V. The MS/MS data were processed as previously described by using MassChemSite (Molecular Discovery Ltd.) and WebChembase [79,80]. Data were plotted with GraphPad Prism and reported as the average ± SD of duplicates.

4.13. Metabolic stability in human liver microsomes

Tested compounds (10 μM, with final 0.1 % DMSO) were pre-incubated for 5 min at 37 °C in a 0.1 M phosphate buffer (pH 7.4) containing HLM (0.5 mg/mL, pool of 10 donors; Merck cat.M0317 Lot #SLCD4026). The reactions were started by addition of 1 mM NADPH. At different time points (0, 5, 15, 30, and 60 min), an aliquot of reactions mixture was taken and quenched with ice-cold acetonitrile 2:1 (containing 1 μM labetalol as an internal standard). Proteins were precipitated by centrifugation at 15,000 g for 10 min at 4 °C (Eppendorf, Italy; centrifuge 5810 R; rotor F-45-30-11), and aliquots of the supernatants were analyzed by LC−MS/MS. Samples were analyzed using Agilent 6540 UHD Accurate-Mass Quadrupole Time-of-Flight (QTOF), equipped with an Agilent 1290 Infinity LC system (Agilent Technologies, Santa Clara, CA, USA). The column was a Phenomenex Luna Omega Polar C18 column (1.6 μm, 2.1 × 150 mm). Column temperature was set at 40 °C and injection volume was 5 μl. The mobile phases consisted of 0.1 % formic acid in water (A) and acetonitrile + 0.1 % formic acid (B) and the LC 20-min gradient elution was as follows: 99.5:0.5 (A/B) to 5:95 (A/B)

over 16 min, 5:95 (A/B) for 4 min, and then reversion back to 99.5:0.5 (A/B) over 2.5 min, at a flow rate of 0.4 ml/min. The Agilent Technology 6540 UHD Accurate Mass Q-TOF LC/MS system was operated under positive conditions with Dual JetStream source (ESI source) in the following conditions: Gas Temp 350 °C, Drying Gas: 9 l/min, Nebulizer: 35 psi, Sheath Gas Temp: 400 °C, Sheath Gas Flow: 9 L/min, Vcap: 4000 V, Nozzle Voltage: 0 V, Fragmentor: 120 V, Skimmer: 65 V, OCT RF Vpp: 750 V. The acquisition was performed in AutoMS/MS mode using an inclusion list to trigger the MS/MS acquisition based on the accurate masses of potential metabolites as computed by MetaSite software (Molecular Discovery Ltd.) [83]. Data Analysis was performed by processing raw data files using Mass-MetaSite (Molecular Discovery Ltd.) and WebMetabase (Molecular Discovery Ltd.).

CRediT authorship contribution statement

Jenny Desantis: Writing – review & editing, Writing – original draft, Methodology, Investigation, Conceptualization. **Alessandro Bazzacco:** Writing – review & editing, Investigation, Formal analysis, Data curation. **Michela Eleuteri:** Writing – review & editing, Investigation, Formal analysis, Data curation. **Sara Tuci:** Writing – review & editing, Investigation, Formal analysis. **Elisa Bianconi:** Investigation. **Antonio Macchiarulo:** Investigation. **Beatrice Mercorelli:** Writing – review & editing, Writing – original draft, Project administration, Methodology, Investigation, Conceptualization. **Arianna Loregian:** Writing – review & editing, Writing – original draft, Supervision, Project administration, Methodology, Investigation, Funding acquisition, Conceptualization. **Laura Goracci:** Writing – review & editing, Writing – original draft, Supervision, Project administration, Methodology, Investigation, Funding acquisition, Conceptualization.

Declaration of competing interest

The authors declare that they have no known competing financial interests or personal relationships that could have appeared to influence the work reported in this paper.

Data availability

Data will be made available on request.

Acknowledgements

This work was supported by Fondazione Cassa di Risparmio di Padova e Rovigo, Italy - Bando Ricerca Covid-2019 Nr. 55777 2020.0162 - "ARREST-COV: AntiviRal PROTAC-Enhanced Small-molecule Therapeutics against COronaViruses" (to A.L.); by Associazione Italiana per la Ricerca sul Cancro, AIRC, Italy, grant IG 2016 - ID. 18855 and grant IG 2021 - ID. 25899 (to A.L.); by Ministero dell'Università e della Ricerca (MIUR), Italy with PRIN 2022 PNRR- cod. P20222YKP8 (to A.L.), PRIN 2022 - cod. 20223RYYFC (to G. Cruciani, A.L. and L.G), and Project "ZODIAC" (to J.D.); by EU funding within the NextGenerationEU-MUR PNRR Extended Partnership initiative on Emerging Infectious Diseases, Project no. PE00000007, INF-ACT (to A. L.); by University of Padua, Italy (PRID 2021 to B.M); and by Molecular Horizon (Italy) within the PRO-CURA project (to L.G.). This publication also received the support of the European Virus Archive Global (EVA-GLOBAL) project that has received funding from the European Union's Horizon 2020 research and innovation programme under grant agreement No. 871029, which provided free access to the SARS-CoV-2/NL/2020 virus.

We thank Prof. Hilgenfeld for kindly providing the pGEX-6P-1-Mpro plasmid, Molecular Horizon srl for support in LC-HRMS analysis and chemical and metabolic stability studies, and Molecular Discovery for support in ternary complexes analyses.

Appendix A. Supplementary data

Supplementary data to this article can be found online at https://doi.org/10.1016/j.ejmech.2024.116202.

Supplementary data

Additional tables containing *in vitro* biological data (Tables S1, S2, and S3) and information regarding the oligonucleotides used for cloning (Table S4); Figures illustrating MST analysis (Figs. S1 and S2) and degradation products (Fig. S3); ^{1}H and ^{13}C NMR spectra of synthesized compounds; HPLC traces of synthesized compounds.

Abbreviations

(BOC) Boceprevir
(BSL3) biosafety level 3
(CoVs) coronaviruses
(DDS) data-dependent scan
(DIPEA) diisopropylethylamine
(DMEM) dulbecco's modified eagle's medium
(FRET) fluorescence resonance energy transfer
(HATU) 1-[bis(dimethylamino)methylene]-1*H*-1,2,3-triazolo[4,5-*b*] pyridinium 3-oxid hexafluorophosphate
(Hyp) hydroxyproline
(INM) indomethacin
(LOD) limit of detection
(LOQ) limit of quantification
(M^{pro}) Main protease
(MST) microscale thermophoresis
(MTT) 3-(4,5-dimethylthiazol-2-yl)-2,5-diphenyl tetrazolium bromide
(NT) non-trasfected
(PGES-2) prostaglandin E synthase type 2
(POI) protein of interest
(PEG) polyethylenglicol
(PRA) plaque reduction assays
(PROTAC) proteolysis targeting chimera
(SI) selectivity index
(TSA) thermal shift analysis
(TLC) thin-layer chromatography
(TPD) targeted protein degradation
(VHL) Von-Hippel Lindau
(WB) western blot

References

[1] K. Garber, The PROTAC gold rush, Nat. Biotechnol. 40 (2022) 12–16, https://doi.org/10.1038/s41587-021-01173-2.
[2] S.B. Alabi, C.M. Crews, Major advances in targeted protein degradation: PROTACs, LYTACs, and MADTACs, J. Biol. Chem. 296 (2021) 100647, https://doi.org/10.1016/j.jbc.2021.100647.
[3] M. He, C. Cao, Z. Ni, Y. Liu, P. Song, S. Hao, Y. He, X. Sun, Y. Rao, PROTACs: great opportunities for academia and industry (an update from 2020 to 2021), Signal Transduct. Targeted Ther. 7 (2022) 181, https://doi.org/10.1038/s41392-022-00999-9.
[4] Y.W. Wang, L. Lan, M. Wang, J.Y. Zhang, Y.H. Gao, L. Shi, L.P. Sun, PROTACS: a technology with a gold rush-like atmosphere, Eur. J. Med. Chem. 247 (2023) 115037, https://doi.org/10.1016/j.ejmech.2022.115037.
[5] (a) D. Li, D. Yu, Y. Li, R. Yang, A bibliometric analysis of PROTAC from 2001 to 2021, Eur. J. Med. Chem 244 (2022) 114838, https://doi.org/10.1016/j.ejmech.2022.114838;
(b) A. Loregian, G. Palù, How academic labs can approach the drug discovery process as a way to synergize with big pharma, Trends Microbiol 21 (2013) 261–264, https://doi.org/10.1016/j.tim.2013.03.006.
[6] M. Bekes, D.R. Langley, C.M. Crews, PROTAC targeted protein degraders: the past is prologue, Nat. Rev. Drug Discov. 21 (2022) 181–200, https://doi.org/10.1038/s41573-021-00371-6.
[7] J.Y. Xi, R.Y. Zhang, K. Chen, L. Yao, M.Q. Li, R. Jiang, X.Y. Li, L. Fan, Advances and perspectives of proteolysis targeting chimeras (PROTACs) in drug discovery, Bioorg. Chem. 125 (2022) 105848, https://doi.org/10.1016/j.bioorg.2022.105848.

[8] K.M. Sakamoto, K.B. Kim, A. Kumagai, F. Mercurio, C.M. Crews, R.J. Deshaies, Protacs: chimeric molecules that target proteins to the Skp1-Cullin-F box complex for ubiquitination and degradation, Proc. Natl. Acad. Sci. U. S. A. 98 (2001) 8554–8559, https://doi.org/10.1073/pnas.141230798.
[9] A. Mullard, Targeted protein degraders crowd into the clinic, Nat. Rev. Drug Discov. 20 (2021) 247–250, https://doi.org/10.1038/d41573-021-00052-4.
[10] Z. Hu, C.M. Crews, Recent developments in PROTAC-mediated protein degradation: from bench to clinic, Chembiochem 23 (2022) e202100270, https://doi.org/10.1002/cbic.202100270.
[11] K. Li, C.M. Crews, PROTACs: past, present and future, Chem. Soc. Rev. 51 (2022) 5214–5236, https://doi.org/10.1039/d2cs00193d.
[12] D. Chirnomas, K.R. Hornberger, C.M. Crews, Protein degraders enter the clinic - a new approach to cancer therapy, Nat. Rev. Clin. Oncol. 20 (2023) 265–278, https://doi.org/10.1038/s41571-023-00736-3.
[13] S. Zeng, Y. Ye, H. Xia, J. Min, J. Xu, Z. Wang, Y. Pan, X. Zhou, W. Huang, Current advances and development strategies of orally bioavailable PROTACs, Eur. J. Med. Chem. 261 (2023) 115793, https://doi.org/10.1016/j.ejmech.2023.115793.
[14] X. Sun, H. Gao, Y. Yang, M. He, Y. Wu, Y. Song, Y. Tong, Y. Rao, PROTACs: great opportunities for academia and industry, Signal Transduct. Targeted Ther. 4 (2019) 64, https://doi.org/10.1038/s41392-019-0101-6.
[15] R.P. Bhole, P.R. Kute, R.V. Chikhale, C.G. Bonde, A. Pant, S.S. Gurav, Unlocking the potential of PROTACs: a comprehensive review of protein degradation strategies in disease therapy, Bioorg. Chem. 139 (2023) 106720, https://doi.org/10.1016/j.bioorg.2023.106720.
[16] Y. Fang, J. Wang, M. Zhao, Q. Zheng, C. Ren, Y. Wang, J. Zhang, Progress and challenges in targeted protein degradation for neurodegenerative disease therapy, J. Med. Chem. 65 (2022) 11454–11477, https://doi.org/10.1021/acs.jmedchem.2c00844.
[17] C. Grohmann, D.S. Marapana, G. Ebert, Targeted protein degradation at the host-pathogen interface, Mol. Microbiol. 117 (2022) 670–681, https://doi.org/10.1111/mmi.14849.
[18] R. Verma, Exploiting ubiquitin ligases for induced target degradation as an antiviral strategy, Adv. Exp. Med. Biol. 1322 (2021) 339–357, https://doi.org/10.1007/978-981-16-0267-2_13.
[19] J. Desantis, L. Goracci, Proteolysis targeting chimeras in antiviral research, Future Med. Chem. 14 (2022) 459–462, https://doi.org/10.4155/fmc-2022-0005.
[20] R.M. Espinoza-Chavez, A. Salerno, A. Liuzzi, A. Ilari, A. Milelli, E. Uliassi, M. L. Bolognesi, Targeted protein degradation for infectious diseases: from basic biology to drug discovery, ACS Bio Med Chem Au 3 (2023) 32–45, https://doi.org/10.1021/acsbiomedchemau.2c00063.
[21] J. Liang, Y. Wu, K. Lan, C. Dong, S. Wu, S. Li, H.B. Zhou, Antiviral PROTACs: opportunity borne with challenge, Cell Insight 2 (2023) 100092, https://doi.org/10.1016/j.cellin.2023.100092.
[22] K. Montrose, G.W. Krissansen, Design of a PROTAC that antagonizes and destroys the cancer-forming X-protein of the hepatitis B virus, Biochem. Biophys. Res. Commun. 453 (2014) 735–740, https://doi.org/10.1016/j.bbrc.2014.10.006.
[23] M. de Wispelaere, G. Du, K.A. Donovan, T. Zhang, N.A. Eleuteri, J.C. Yuan, J. Kalabathula, R.P. Nowak, E.S. Fischer, N.S. Gray, P.L. Yang, Small molecule degraders of the hepatitis C virus protease reduce susceptibility to resistance mutations, Nat. Commun. 10 (2019) 3468, https://doi.org/10.1038/s41467-019-11429-w.
[24] Y. Liu, C. Liang, L. Xin, X. Ren, L. Tian, X. Ju, H. Li, Y. Wang, Q. Zhao, H. Liu, W. Cao, X. Xie, D. Zhang, Y. Wang, Y. Jian, The development of Coronavirus 3C-Like protease (3CL(pro)) inhibitors from 2010 to 2020, Eur. J. Med. Chem. 206 (2020) 112711, https://doi.org/10.1016/j.ejmech.2020.112711.
[25] W. Martinez-Ortiz, M.M. Zhou, Could PROTACs protect us from COVID-19? Drug Discov. Today 25 (2020) 1894–1896, https://doi.org/10.1016/j.drudis.2020.08.007.
[26] M. Shaheer, R. Singh, M.E. Sobhia, Protein degradation: a novel computational approach to design protein degrader probes for main protease of SARS-CoV-2, J. Biomol. Struct. Dyn. 40 (2022) 10905–10917, https://doi.org/10.1080/07391102.2021.1953601.
[27] J. Desantis, B. Mercorelli, M. Celegato, F. Croci, A. Bazzacco, M. Baroni, L. Siragusa, G. Cruciani, A. Loregian, L. Goracci, Indomethacin-based PROTACs as pan-coronavirus antiviral agents, Eur. J. Med. Chem. 226 (2021) 113814, https://doi.org/10.1016/j.ejmech.2021.113814.
[28] F. Hahn, S.T. Hamilton, C. Wangen, M. Wild, J. Kicuntod, N. Bruckner, J.E. L. Follett, L. Herrmann, A. Kheimar, B.B. Kaufer, W.D. Rawlinson, S.B. Tsogoeva, M. Marschall, Development of a PROTAC-based targeting strategy provides a mechanistically unique mode of anti-cytomegalovirus activity, Int. J. Mol. Sci. 22 (2021), https://doi.org/10.3390/ijms222312858.
[29] H. Li, S. Wang, W. Ma, B. Cheng, Y. Yi, X. Ma, S. Xiao, L. Zhang, D. Zhou, Discovery of pentacyclic triterpenoid PROTACs as a class of effective hemagglutinin protein degraders, J. Med. Chem. 65 (2022) 7154–7169, https://doi.org/10.1021/acs.jmedchem.1c02013.
[30] Z. Xu, X. Liu, X. Ma, W. Zou, Q. Chen, F. Chen, X. Deng, J. Liang, C. Dong, K. Lan, S. Wu, H.B. Zhou, Discovery of oseltamivir-based novel PROTACs as degraders targeting neuraminidase to combat H1N1 influenza virus, Cell Insight 1 (2022) 100030, https://doi.org/10.1016/j.cellin.2022.100030.
[31] F. Rizvi, A.M. Khan, A.W. Ansari, K. Ali, A.M. Khan, F.M. Khan, Different variants of SARS-CoV-2: a comprehensive review on mutation patterns and pathogenicity, Coronaviruses 4 (2023) 22–32, https://doi.org/10.2174/2666796704666230328171636.
[32] Y. Mutoh, T. Umemura, T. Nishikawa, K. Kondo, Y. Nishina, K. Soejima, Y. Noguchi, T. Bando, S. Ota, T. Shimahara, S. Hirota, S. Hagimoto, R. Takei, J. Fukihara, H. Sasano, Y. Yamano, T. Yokoyama, K. Kataoka, T. Matsuda, T. Kimura, T. Ichihara, Y. Kondoh, Real-world experience of the comparative effectiveness and safety of molnupiravir and nirmatrelvir/ritonavir in high-risk patients with COVID-19 in a community setting, Viruses 15 (2023), https://doi.org/10.3390/v15030811.
[33] S. Aboul-Fotouh, A.N. Mahmoud, E.M. Elnahas, M.Z. Habib, S.M. Abdelraouf, What are the current anti-COVID-19 drugs? From traditional to smart molecular mechanisms, Virol. J. 20 (2023) 241, https://doi.org/10.1186/s12985-023-02210-z.
[34] A.K. Ghosh, M. Brindisi, D. Shahabi, M.E. Chapman, A.D. Mesecar, Drug development and medicinal chemistry efforts toward SARS-coronavirus and Covid-19 therapeutics, ChemMedChem 15 (2020) 907–932, https://doi.org/10.1002/cmdc.202000223.
[35] J.S. Morse, T. Lalonde, S. Xu, W.R. Liu, Learning from the past: possible urgent prevention and treatment options for severe acute respiratory infections caused by 2019-nCoV, Chembiochem 21 (2020) 730–738, https://doi.org/10.1002/cbic.202000047.
[36] A. Sha, Y. Liu, H. Hao, Current state-of-the-art and potential future therapeutic drugs against COVID-19, Front. Cell Dev. Biol. 11 (2023) 1238027, https://doi.org/10.3389/fcell.2023.1238027.
[37] G. Li, R. Hilgenfeld, R. Whitley, E. De Clercq, Therapeutic strategies for COVID-19: progress and lessons learned, Nat. Rev. Drug Discov. 22 (2023) 449–475, https://doi.org/10.1038/s41573-023-00672-y.
[38] A. Citarella, A. Dimasi, D. Moi, D. Passarella, A. Scala, A. Piperno, N. Micale, Recent advances in SARS-CoV-2 main protease inhibitors: from nirmatrelvir to future perspectives, Biomolecules 13 (2023), https://doi.org/10.3390/biom13091339.
[39] X. Li, Y. Song, Structure and function of SARS-CoV and SARS-CoV-2 main proteases and their inhibition: a comprehensive review, Eur. J. Med. Chem. 260 (2023) 115772, https://doi.org/10.1016/j.ejmech.2023.115772.
[40] N.D. Kushwaha, J. Mohan, B. Kushwaha, T. Ghazi, J.C. Nwabuife, N. Koorbanally, A.A. Chuturgoon, A comprehensive review on the global efforts on vaccines and repurposed drugs for combating COVID-19, Eur. J. Med. Chem. 260 (2023) 115719, https://doi.org/10.1016/j.ejmech.2023.115719.
[41] Y. Duan, H. Wang, Z. Yuan, H. Yang, Structural biology of SARS-CoV-2 M(pro) and drug discovery, Curr. Opin. Struct. Biol. 82 (2023) 102667, https://doi.org/10.1016/j.sbi.2023.102667.
[42] Z. She, Y. Yao, C. Wang, Y. Li, X. Xiong, Y. Liu, M(pro)-targeted anti-SARS-CoV-2 inhibitor-based drugs, J. Chem. Res. 47 (2023) 17475198231184799, https://doi.org/10.1177/17475198231184799.
[43] X. Pang, W. Xu, Y. Liu, H. Li, L. Chen, The research progress of SARS-CoV-2 main protease inhibitors from 2020 to 2022, Eur. J. Med. Chem. 257 (2023) 115491, https://doi.org/10.1016/j.ejmech.2023.115491.
[44] T. Kronenberger, S.A. Laufer, T. Pillaiyar, COVID-19 therapeutics: small-molecule drug development targeting SARS-CoV-2 main protease, Drug Discov. Today 28 (2023) 103579, https://doi.org/10.1016/j.drudis.2023.103579.
[45] S. Gao, L. Song, K. Sylvester, B. Mercorelli, A. Loregian, K. Toth, R.H. Weisse, A. Useini, N. Strater, M. Yang, B. Ye, A.E. Tollefson, C.E. Muller, X. Liu, P. Zhan, Design, synthesis, and biological evaluation of trisubstituted piperazine derivatives as noncovalent severe acute respiratory syndrome coronavirus 2 main protease inhibitors with improved antiviral activity and favorable druggability, J. Med. Chem. (2023), https://doi.org/10.1021/acs.jmedchem.3c01876.
[46] H. Tan, Y. Hu, P. Jadhav, B. Tan, J. Wang, Progress and challenges in targeting the SARS-CoV-2 papain-like protease, J. Med. Chem. 65 (2022) 7561–7580, https://doi.org/10.1021/acs.jmedchem.2c00303.
[47] X. Li, Y. Song, Targeting SARS-CoV-2 nonstructural protein 3: function, structure, inhibition, and perspective in drug discovery, Drug Discov. Today 29 (2023) 103832, https://doi.org/10.1016/j.drudis.2023.103832.
[48] C.S. Brian Chia, S. Pheng Lim, A patent review on SARS Coronavirus papain-like protease (PL(pro)) inhibitors, ChemMedChem 18 (2023) e202300216, https://doi.org/10.1002/cmdc.202300216.
[49] M.S. Bekheit, S.S. Panda, A.S. Girgis, Potential RNA-dependent RNA polymerase (RdRp) inhibitors as prospective drug candidates for SARS-CoV-2, Eur. J. Med. Chem. 252 (2023) 115292, https://doi.org/10.1016/j.ejmech.2023.115292.
[50] X. Xu, Y. Chen, X. Lu, W. Zhang, W. Fang, L. Yuan, X. Wang, An update on inhibitors targeting RNA-dependent RNA polymerase for COVID-19 treatment: promises and challenges, Biochem. Pharmacol. 205 (2022) 115279, https://doi.org/10.1016/j.bcp.2022.115279.
[51] A. Wu, K. Shi, J. Wang, R. Zhang, Y. Wang, Targeting SARS-CoV-2 entry processes: the promising potential and future of host-targeted small-molecule inhibitors, Eur. J. Med. Chem. 263 (2024) 115923, https://doi.org/10.1016/j.ejmech.2023.115923.
[52] D. Tam, A.C. Lorenzo-Leal, L.R. Hernandez, H. Bach, Targeting SARS-CoV-2 non-structural proteins, Int. J. Mol. Sci. 24 (2023), https://doi.org/10.3390/ijms241613002.
[53] C. Amici, A. Di Caro, A. Ciucci, L. Chiappa, C. Castilletti, V. Martella, N. Decaro, C. Buonavoglia, M.R. Capobianchi, M.G. Santoro, Indomethacin has a potent antiviral activity against SARS coronavirus, Antivir. Ther. 11 (2006) 1021–1030.
[54] A.E. Reynolds, L.W. Enquist, Biological interactions between herpesviruses and cyclooxygenase enzymes, Rev. Med. Virol. 16 (2006) 393–403, https://doi.org/10.1002/rmv.519.
[55] J. Schroer, T. Shenk, Inhibition of cyclooxygenase activity blocks cell-to-cell spread of human cytomegalovirus, Proc. Natl. Acad. Sci. U. S. A. 105 (2008) 19468–19473, https://doi.org/10.1073/pnas.0810740105.
[56] H. Bahrami, N.E. Daryani, B. Haghpanah, A. Moayyeri, K.F. Moghadam, S. Mirmomen, F. Kamangar, Effects of indomethacin on viral replication markers

in asymptomatic carriers of hepatitis B: a randomized, placebo-controlled trial, Am. J. Gastroenterol. 100 (2005) 856–861, https://doi.org/10.1111/j.1572-0241.2005.41144.x.
[57] P. Kiani, A. Scholey, T.A. Dahl, L. McMann, J.M. Iversen, J.C. Verster, In vitro assessment of the antiviral activity of ketotifen, indomethacin and naproxen, alone and in combination, against SARS-CoV-2, Viruses (2021) 13, https://doi.org/10.3390/v13040558.
[58] N. Shekhar, H. Kaur, P. Sarma, A. Prakash, B. Medhi, Indomethacin: an exploratory study of antiviral mechanism and host-pathogen interaction in COVID-19, Expert Rev. Anti Infect. Ther. 20 (2022) 383–390, https://doi.org/10.1080/14787210.2022.1990756.
[59] R. Chakraborty, G. Bhattacharje, J. Baral, B. Manna, J. Mullick, B.S. Mathapati, P. Abraham, J. M, Y. Hasija, A. Ghosh, A.K. Das, In-silico screening and in-vitro assay show the antiviral effect of Indomethacin against SARS-CoV-2, Comput. Biol. Med. 147 (2022) 105788, https://doi.org/10.1016/j.compbiomed.2022.105788.
[60] R. Ravichandran, S.K. Mohan, S.K. Sukumaran, D. Kamaraj, S.S. Daivasuga, S. Ravi, S. Vijayaraghavalu, R.K. Kumar, An open label randomized clinical trial of Indomethacin for mild and moderate hospitalised Covid-19 patients, Sci. Rep. 12 (2022) 6413, https://doi.org/10.1038/s41598-022-10370-1.
[61] D.E. Gordon, J. Hiatt, M. Bouhaddou, V.V. Rezelj, S. Ulferts, H. Braberg, A. S. Jureka, K. Obernier, J.Z. Guo, J. Batra, R.M. Kaake, A.R. Weckstein, T. W. Owens, M. Gupta, S. Pourmal, E.W. Titus, M. Cakir, M. Soucheray, M. McGregor, Z. Cakir, G. Jang, M.J. O'Meara, T.A. Tummino, Z. Zhang, H. Foussard, A. Rojc, Y. Zhou, D. Kuchenov, R. Huttenhain, J. Xu, M. Eckhardt, D. L. Swaney, J.M. Fabius, M. Ummadi, B. Tutuncuoglu, U. Rathore, M. Modak, P. Haas, K.M. Haas, Z.Z.C. Naing, E.H. Pulido, Y. Shi, I. Barrio-Hernandez, D. Memon, E. Petsalaki, A. Dunham, M.C. Marrero, D. Burke, C. Koh, T. Vallet, J. A. Silvas, C.M. Azumaya, C. Billesbolle, A.F. Brilot, M.G. Campbell, A. Diallo, M. S. Dickinson, D. Diwanji, N. Herrera, N. Hoppe, H.T. Kratochvil, Y. Liu, G.E. Merz, M. Moritz, H.C. Nguyen, C. Nowotny, C. Puchades, A.N. Rizo, U. Schulze-Gahmen, A.M. Smith, M. Sun, I.D. Young, J. Zhao, D. Asarnow, J. Biel, A. Bowen, J.R. Braxton, J. Chen, C.M. Chio, U.S. Chio, I. Deshpande, L. Doan, B. Faust, S. Flores, M. Jin, K. Kim, V.L. Lam, F. Li, J. Li, Y.L. Li, Y. Li, X. Liu, M. Lo, K. E. Lopez, A.A. Melo, F.R. Moss 3rd, P. Nguyen, J. Paulino, K.I. Pawar, J.K. Peters, T.H. Pospiech Jr., M. Safari, S. Sangwan, K. Schaefer, P.V. Thomas, A.C. Thwin, R. Trenker, E. Tse, T.K.M. Tsui, F. Wang, N. Whitis, Z. Yu, K. Zhang, Y. Zhang, F. Zhou, D. Saltzberg, Q.S.B. Consortium, A.J. Hodder, A.S. Shun-Shion, D. M. Williams, K.M. White, R. Rosales, T. Kehrer, L. Miorin, E. Moreno, A.H. Patel, S. Rihn, M.M. Khalid, A. Vallejo-Gracia, P. Fozouni, C.R. Simoneau, T.L. Roth, D. Wu, M.A. Karim, M. Ghoussaini, I. Dunham, F. Berardi, S. Weigang, M. Chazal, J. Park, J. Logue, M. McGrath, S. Weston, R. Haupt, C.J. Hastie, M. Elliott, F. Brown, K.A. Burness, E. Reid, M. Dorward, C. Johnson, S.G. Wilkinson, A. Geyer, D.M. Giesel, C. Baillie, S. Raggett, H. Leech, R. Toth, N. Goodman, K. C. Keough, A.L. Lind, C. Zoonomia, R.J. Klesh, K.R. Hemphill, J. Carlson-Stevermer, J. Oki, K. Holden, T. Maures, K.S. Pollard, A. Sali, D.A. Agard, Y. Cheng, J.S. Fraser, A. Frost, N. Jura, T. Kortemme, A. Manglik, D. R. Southworth, R.M. Stroud, D.R. Alessi, P. Davies, M.B. Frieman, T. Ideker, C. Abate, N. Jouvenet, G. Kochs, B. Shoichet, M. Ott, M. Palmarini, K.M. Shokat, A. Garcia-Sastre, J.A. Rassen, R. Grosse, O.S. Rosenberg, K.A. Verba, C.F. Basler, M. Vignuzzi, A.A. Peden, P. Beltrao, N.J. Krogan, Comparative host-coronavirus protein interaction networks reveal pan-viral disease mechanisms, Science 370 (2020), https://doi.org/10.1126/science.abe9403.
[62] D.E. Gordon, G.M. Jang, M. Bouhaddou, J. Xu, K. Obernier, K.M. White, M. J. O'Meara, V.V. Rezelj, J.Z. Guo, D.L. Swaney, T.A. Tummino, R. Huttenhain, R. M. Kaake, A.L. Richards, B. Tutuncuoglu, H. Foussard, J. Batra, K. Haas, M. Modak, M. Kim, P. Haas, B.J. Polacco, H. Braberg, J.M. Fabius, M. Eckhardt, M. Soucheray, M.J. Bennett, M. Cakir, M.J. McGregor, Q. Li, B. Meyer, F. Roesch, T. Vallet, A. Mac Kain, L. Miorin, E. Moreno, Z.Z.C. Naing, Y. Zhou, S. Peng, Y. Shi, Z. Zhang, W. Shen, I.T. Kirby, J.E. Melnyk, J.S. Chorba, K. Lou, S.A. Dai, I. Barrio-Hernandez, D. Memon, C. Hernandez-Armenta, J. Lyu, C.J.P. Mathy, T. Perica, K.B. Pilla, S.J. Ganesan, D.J. Saltzberg, R. Rakesh, X. Liu, S. B. Rosenthal, L. Calviello, S. Venkataramanan, J. Liboy-Lugo, Y. Lin, X.P. Huang, Y. Liu, S.A. Wankowicz, M. Bohn, M. Safari, F.S. Ugur, C. Koh, N.S. Savar, Q. D. Tran, D. Shengjuler, S.J. Fletcher, M.C. O'Neal, Y. Cai, J.C.J. Chang, D. J. Broadhurst, S. Klippsten, P.P. Sharp, N.A. Wenzell, D. Kuzuoglu-Ozturk, H. Y. Wang, R. Trenker, J.M. Young, D.A. Cavero, J. Hiatt, T.L. Roth, U. Rathore, A. Subramanian, J. Noack, M. Hubert, R.M. Stroud, A.D. Frankel, O.S. Rosenberg, K.A. Verba, D.A. Agard, M. Ott, M. Emerman, N. Jura, M. von Zastrow, E. Verdin, A. Ashworth, O. Schwartz, C. d'Enfert, S. Mukherjee, M. Jacobson, H.S. Malik, D. G. Fujimori, T. Ideker, C.S. Craik, S.N. Floor, J.S. Fraser, J.D. Gross, A. Sali, B. L. Roth, D. Ruggero, J. Taunton, T. Kortemme, P. Beltrao, M. Vignuzzi, A. Garcia-Sastre, K.M. Shokat, B.K. Shoichet, N.J. Krogan, A SARS-CoV-2 protein interaction map reveals targets for drug repurposing, Nature 583 (2020) 459–468, https://doi.org/10.1038/s41586-020-2286-9.
[63] R.A. Al-Horani, S. Kar, Potential anti-SARS-CoV-2 therapeutics that target the post-entry stages of the viral life cycle: a comprehensive review, Viruses (2020) 12, https://doi.org/10.3390/v12101092.
[64] S. Ljubin-Sternak, T. Mestrovic, I. Luksic, M. Mijac, J. Vranes, Seasonal coronaviruses and other neglected respiratory viruses: a global perspective and a local snapshot, Front. Public Health 9 (2021) 691163, https://doi.org/10.3389/fpubh.2021.691163.
[65] L. Goracci, J. Desantis, A. Valeri, B. Castellani, M. Eleuteri, G. Cruciani, Understanding the metabolism of proteolysis targeting chimeras (PROTACs): the next step toward pharmaceutical applications, J. Med. Chem. 63 (2020) 11615–11638, https://doi.org/10.1021/acs.jmedchem.0c00793.
[66] J. Desantis, A. Mammoli, M. Eleuteri, A. Coletti, F. Croci, A. Macchiarulo, L. Goracci, PROTACs bearing piperazine-containing linkers: what effect on their protonation state? RSC Adv. 12 (2022) 21968–21977, https://doi.org/10.1039/d2ra03761k.
[67] A. Kannt, I. Dikic, Expanding the arsenal of E3 ubiquitin ligases for proximity-induced protein degradation, Cell Chem. Biol. 28 (2021) 1014–1031, https://doi.org/10.1016/j.chembiol.2021.04.007.
[68] B.E. Smith, S.L. Wang, S. Jaime-Figueroa, A. Harbin, J. Wang, B.D. Hamman, C. M. Crews, Differential PROTAC substrate specificity dictated by orientation of recruited E3 ligase, Nat. Commun. 10 (2019) 131, https://doi.org/10.1038/s41467-018-08027-7.
[69] T. Ishida, A. Ciulli, E3 ligase ligands for PROTACs: how they were found and how to discover new ones, SLAS Discov 26 (2021) 484–502, https://doi.org/10.1177/2472555220965528.
[70] S.C. Gnoatto, A. Dassonville-Klimpt, S. Da Nascimento, P. Galera, K. Boumediene, G. Gosmann, P. Sonnet, S. Moslemi, Evaluation of ursolic acid isolated from Ilex paraguariensis and derivatives on aromatase inhibition, Eur. J. Med. Chem. 43 (2008) 1865–1877, https://doi.org/10.1016/j.ejmech.2007.11.021.
[71] D.P. Bondeson, A. Mares, I.E. Smith, E. Ko, S. Campos, A.H. Miah, K. E. Mulholland, N. Routly, D.L. Buckley, J.L. Gustafson, N. Zinn, P. Grandi, S. Shimamura, G. Bergamini, M. Faelth-Savitski, M. Bantscheff, C. Cox, D. A. Gordon, R.R. Willard, J.J. Flanagan, L.N. Casillas, B.J. Votta, W. den Besten, K. Famm, L. Kruidenier, P.S. Carter, J.D. Harling, I. Churcher, C.M. Crews, Catalytic in vivo protein knockdown by small-molecule PROTACs, Nat. Chem. Biol. 11 (2015) 611–617, https://doi.org/10.1038/nchembio.1858.
[72] K. Raina, J. Lu, Y. Qian, M. Altieri, D. Gordon, A.M. Rossi, J. Wang, X. Chen, H. Dong, K. Siu, J.D. Winkler, A.P. Crew, C.M. Crews, K.G. Coleman, PROTAC-induced BET protein degradation as a therapy for castration-resistant prostate cancer, Proc. Natl. Acad. Sci. U. S. A. 113 (2016) 7124–7129, https://doi.org/10.1073/pnas.1521738113.
[73] L. Fu, J. Zhang, B. Shen, L. Kong, Y. Liu, W. Tu, W. Wang, X. Cai, X. Wang, N. Cheng, M. Xia, T. Zhou, Q. Liu, Y. Xu, J. Yang, P. Gavine, U. Philippar, R. Attar, J.P. Edwards, J.D. Venable, X. Dai, Discovery of highly potent and selective IRAK1 degraders to probe scaffolding functions of IRAK1 in ABC DLBCL, J. Med. Chem. 64 (2021) 10878–10889, https://doi.org/10.1021/acs.jmedchem.1c00103.
[74] W. Yan, B.S. Pan, J. Shao, H.K. Lin, H.Y. Li, Feasible column chromatography-free, multi-gram scale synthetic process of VH032 amine, which could enable rapid PROTAC library construction, ACS Omega 7 (2022) 26015–26020, https://doi.org/10.1021/acsomega.2c00245.
[75] B. Mercorelli, J. Desantis, M. Celegato, A. Bazzacco, L. Siragusa, P. Benedetti, M. Eleuteri, F. Croci, G. Cruciani, L. Goracci, A. Loregian, Discovery of novel SARS-CoV-2 inhibitors targeting the main protease M(pro) by virtual screenings and hit optimization, Antivir. Res. 204 (2022) 105350, https://doi.org/10.1016/j.antiviral.2022.105350.
[76] L. Siragusa, S. Cross, M. Baroni, L. Goracci, G. Cruciani, BioGPS: navigating biological space to predict polypharmacology, off-targeting, and selectivity, Proteins 83 (2015) 517–532, https://doi.org/10.1002/prot.24753.
[77] E. Bianconi, A. Gidari, M. Souma, S. Sabbatini, D. Grifagni, C. Bigiotti, E. Schiaroli, L. Comez, A. Paciaroni, F. Cantini, D. Francisci, A. Macchiarulo, The hope and hype of ellagic acid and urolithins as ligands of SARS-CoV-2 Nsp5 and inhibitors of viral replication, J. Enzym. Inhib. Med. Chem. 38 (2023), https://doi.org/10.1080/14756366.2023.2251721.
[78] Y. Zhu, J. Binder, I. Yurgelonis, D.K. Rai, S. Lazarro, C. Costales, K. Kobylarz, P. McMonagle, C.M. Steppan, L. Aschenbrenner, A.S. Anderson, R.D. Cardin, Generation of a VeroE6 Pgp gene knock out cell line and its use in SARS-CoV-2 antiviral study, Antivir. Res. 208 (2022) 105429, https://doi.org/10.1016/j.antiviral.2022.105429.
[79] S. Bonciarelli, J. Desantis, S. Cerquiglini, L. Goracci, MassChemSite for in-depth forced degradation analysis of PARP inhibitors olaparib, rucaparib, and niraparib, ACS Omega 8 (2023) 7005–7016, https://doi.org/10.1021/acsomega.2c07815.
[80] S. Bonciarelli, J. Desantis, L. Goracci, L. Siragusa, I. Zamora, E. Ortega-Carrasco, Automatic identification of lansoprazole degradants under stress conditions by LC-HRMS with MassChemSite and WebChembase, J. Chem. Inf. Model. 61 (2021) 2706–2719, https://doi.org/10.1021/acs.jcim.1c00226.
[81] B. Bonn, C. Leandersson, F. Fontaine, I. Zamora, Enhanced metabolite identification with MS(E) and a semi-automated software for structural elucidation, Rapid Commun. Mass Spectrom. 24 (2010) 3127–3138, https://doi.org/10.1002/rcm.4753.
[82] I. Zamora, F. Fontaine, B. Serra, G. Plasencia, High-throughput, computer assisted, specific MetID. A revolution for drug discovery, Drug Discov. Today Technol. 10 (2013) e199–e205, https://doi.org/10.1016/j.ddtec.2012.10.015.
[83] S. Strano-Rossi, L. Anzillotti, S. Dragoni, R.M. Pellegrino, L. Goracci, V.L. Pascali, G. Cruciani, Metabolism of JWH-015, JWH-098, JWH-251, and JWH-307 in silico and in vitro: a pilot study for the detection of unknown synthetic cannabinoids metabolites, Anal. Bioanal. Chem. 406 (2014) 3621–3636, https://doi.org/10.1007/s00216-014-7793-9.
[84] A. Brink, F. Fontaine, M. Marschmann, B. Steinhuber, E.N. Cece, I. Zamora, A. Pahler, Post-acquisition analysis of untargeted accurate mass quadrupole time-of-flight MS(E) data for multiple collision-induced neutral losses and fragment ions of glutathione conjugates, Rapid Commun. Mass Spectrom. 28 (2014) 2695–2703, https://doi.org/10.1002/rcm.7062.
[85] T. Radchenko, F. Fontaine, L. Morettoni, I. Zamora, WebMetabase: cleavage sites analysis tool for natural and unnatural substrates from diverse data source, Bioinformatics 35 (2019) 650–655, https://doi.org/10.1093/bioinformatics/bty667.

[86] L. Tian, T. Qiang, X. Yang, Y. Gao, X. Zhai, K. Kang, C. Du, Q. Lu, H. Gao, D. Zhang, X. Xie, C. Liang, Development of de-novo coronavirus 3-chymotrypsin-like protease (3CL(pro)) inhibitors since COVID-19 outbreak: a strategy to tackle challenges of persistent virus infection, Eur. J. Med. Chem. 264 (2023) 115979, https://doi.org/10.1016/j.ejmech.2023.115979.
[87] X. Sang, J. Wang, J. Zhou, Y. Xu, J. An, A. Warshel, Z. Huang, A chemical strategy for the degradation of the main protease of SARS-CoV-2 in cells, J. Am. Chem. Soc. (2023), https://doi.org/10.1021/jacs.3c12678.
[88] C.I. Fincham, A. Bressan, P. D'Andrea, A. Ettorre, S. Giuliani, S. Mauro, S. Meini, M. Paris, L. Quartara, C. Rossi, A. Squarcia, C. Valenti, F. Daniela, C.A. Maggi, Design and synthesis of novel sulfonamide-containing bradykinin hB(2) receptor antagonists. Synthesis and structure-relationships of alpha,alpha-tetrahydropyranylglycine, Bioorg. Med. Chem. 20 (2012) 2091–2100, https://doi.org/10.1016/j.bmc.2012.01.036.
[89] M.A. Cinelli, B. Cordero, T.S. Dexheimer, Y. Pommier, M. Cushman, Synthesis and biological evaluation of 14-(aminoalkyl-aminomethyl)aromathecins as topoisomerase I inhibitors: investigating the hypothesis of shared structure-activity relationships, Bioorg. Med. Chem. 17 (2009) 7145–7155, https://doi.org/10.1016/j.bmc.2009.08.066.
[90] A. Loregian, B. Mercorelli, G. Muratore, E. Sinigalia, S. Pagni, S. Massari, S. G. Gribaudo, B. Gatto, M. Palumbo, O. Tabarrini, V. Cecchetti, G. Palù, The 6-aminoquinolone WC5 inhibits human cytomegalovirus replication at an early stage by interfering with the transactivating activity of viral immediate-early 2 protein, Antimicrob. Agents Chemother 54 (2010) 1930–1940, https://doi.org/10.1128/AAC.01730-09.
[91] B. Mercorelli, A. Luganini, G. Nannetti, O. Tabarrini, G. Palu, G. Gribaudo, A. Loregian, Drug repurposing approach identifies inhibitors of the prototypic viral transcription factor IE2 that block human cytomegalovirus replication, Cell Chem. Biol. 23 (2016) 340–351, https://doi.org/10.1016/j.chembiol.2015.12.012.
[92] L. Zhang, D. Lin, X. Sun, U. Curth, C. Drosten, L. Sauerhering, S. Becker, K. Rox, R. Hilgenfeld, Crystal structure of SARS-CoV-2 main protease provides a basis for design of improved alpha-ketoamide inhibitors, Science 368 (2020) 409–412, https://doi.org/10.1126/science.abb3405.
[93] H.M. Berman, J. Westbrook, Z. Feng, G. Gilliland, T.N. Bhat, H. Weissig, I. N. Shindyalov, P.E. Bourne, The protein Data Bank, Nucleic Acids Res. 28 (2000) 235–242, https://doi.org/10.1093/nar/28.1.235.
[94] M. Baroni, G. Cruciani, S. Sciabola, F. Perruccio, J.S. Mason, A common reference framework for analyzing/comparing proteins and ligands. Fingerprints for Ligands and Proteins (FLAP): theory and application, J. Chem. Inf. Model. 47 (2007) 279–294, https://doi.org/10.1021/ci600253e.
[95] S. Cross, M. Baroni, E. Carosati, P. Benedetti, S. Clementi, FLAP: GRID molecular interaction fields in virtual screening. validation using the DUD data set, J. Chem. Inf. Model. 50 (2010) 1442–1450, https://doi.org/10.1021/ci100221g.
[96] M.S. Gadd, A. Testa, X. Lucas, K.H. Chan, W. Chen, D.J. Lamont, M. Zengerle, A. Ciulli, Structural basis of PROTAC cooperative recognition for selective protein degradation, Nat. Chem. Biol. 13 (2017) 514–521, https://doi.org/10.1038/nchembio.2329.
[97] E. Carosati, S. Sciabola, G. Cruciani, Hydrogen bonding interactions of covalently bonded fluorine atoms: from crystallographic data to a new angular function in the GRID force field, J. Med. Chem. 47 (2004) 5114–5125, https://doi.org/10.1021/jm0498349.
[98] P.J. Goodford, A computational procedure for determining energetically favorable binding sites on biologically important macromolecules, J. Med. Chem. 28 (1985) 849–857, https://doi.org/10.1021/jm00145a002.
[99] www.moldiscovery.com/software/grid.
[100] J.S. Mason, A. Bortolato, D.R. Weiss, F. Deflorian, B. Tehan, F.H. Marshall, High end GPCR design: crafted ligand design and druggability analysis using protein structure, lipophilic hotspots and explicit water networks, Silico Pharmacol 1 (23) (2013), https://doi.org/10.1186/2193-9616-1-23.
[101] https://www.sigmaaldrich.com/deepweb/assets/sigmaaldrich/product/documents/103/938/an1730en00.pdf.